

Under-ice acoustic navigation using real-time model-aided range estimation

EeShan C. Bhatt,^{1, a} Oscar Viquez,¹ and Henrik Schmidt¹

*Department of Mechanical Engineering, Massachusetts Institute of Technology,
Cambridge, MA*

(Dated: 31 March 2022)

1 The long baseline (LBL) underwater navigation paradigm relies on the conversion
2 of travel times into pseudoranges to trilaterate position. For real-time autonomous
3 underwater vehicle (AUV) operations, this conversion assumes an isovelocity sound
4 speed. For re-navigation, computationally and/or labor intensive acoustic model-
5 ing may be employed to reduce uncertainty. This work demonstrates a real-time
6 ray-based prediction method of the effective sound speed along a path from source
7 to receiver to minimize pseudorange error. This method was implemented for an
8 AUV-LBL system in the Beaufort Sea, in total ice-covered conditions and a double-
9 ducted propagation environment. Given the lack of Global Navigation Satellite Sys-
10 tem (GNSS) data throughout the vehicle's mission, the pseudorange performance is
11 first evaluated on acoustic transmissions between GNSS-linked beacons. The mean
12 real-time absolute range error between beacons is roughly 11 m at distances up to
13 3 km. A consistent overestimation in the real-time method provides insights for
14 improved eigenray filtering by the number of bounces. An operationally equivalent
15 pipeline is used to re-position the LBL beacons and re-navigate the AUV, using mod-
16 eled, historical, and locally observed sound speed profiles. The best re-navigation er-
17 rror is 1.84 ± 2.19 m rms. The improved performance suggests this approach extends
18 the single meter accuracy of the deployed GNSS units into the water column.

^aebhatt@whoi.edu

¹⁹ **I. INTRODUCTION**

²⁰ Autonomous underwater vehicles (AUVs) are increasingly capable platforms to explore
²¹ and sample the ocean, particularly for remote and/or dangerous regions. However, navi-
²² gation uncertainty is a major challenge in considering AUVs as standard tools for oceano-
²³ graphic research. While land and air-based robots utilize information from Global Nav-
²⁴ igation Satellite Systems (GNSS) to achieve single-meter location accuracy and precision
²⁵ throughout the duration of their missions, AUVs cannot access GNSS fixes while under-
²⁶ water. Therefore, underwater vehicles have relied on any combination of dead reckoning,
²⁷ hydrodynamic models, inertial navigation systems, doppler velocity logs, and acoustic base-
²⁸ line positioning systems for navigation ([Paull *et al.*, 2014](#)). Limiting navigation error and
²⁹ drift requires an AUV to periodically stall on the surface and obtain a GNSS fix to re-
³⁰ set its position error. This foolproof method of self-positioning is undesirable for stealth,
³¹ adverse weather conditions, and mission efficiency, and inaccessible in a GNSS-denied sit-
³² uation like an ice-covered environment. Of underwater acoustic navigation systems, long
³³ baseline (LBL) is the most GNSS-like in style and scale, and most appropriate for mitigat-
³⁴ ing drift without overburdening computation or payload size on the vehicle ([Van Uffelen,](#)
³⁵ [2021](#)). The state-of-the-art for LBL outsources depth to a pressure sensor and solves the
³⁶ two-dimensional localization problem with an isovelocity, linear scaling between one-way
³⁷ travel time (OWTT) and range ([Eustice *et al.*, 2006, 2007; Webster *et al.*, 2009, 2012](#)).

³⁸ This assumption is valid for small-scale operations but oversimplifies propagation at larger
³⁹ scales or complex sound speed structure. To achieve single meter, GNSS-like performance

40 in a GNSS-denied environment, we demonstrate an embedded ray-based data processing
 41 algorithm to convert recorded OWTTs into pseudorange estimates. An *in situ* sound speed
 42 profile (SSP) is used despite the small operational domain because of the relatively high-risk
 43 mission environment—total under-ice conditions and a variable double-ducted acoustic envi-
 44 ronment. This methodology was integrated onto the AUV *Macrura*, deployed and recovered
 45 in the Beaufort Sea, in March 2020, during the Ice Exercise 2020 (ICEX20).

46 For consistency, we delineate specific definitions for timing, positioning, and navigation
 47 from [Howe et al. \(2019\)](#).

- 48 1. Timing is the ability to acquire and maintain accurate and precise time anywhere in
 49 the domain of interest within user-defined timeliness parameters
- 50 2. Positioning is the ability to accurately and precisely determine one's location refer-
 51 enced to a standard geodetic system
- 52 3. Navigation is the ability to determine current and desired position (relative or absolute)
 53 and apply corrections to course, orientation, and speed to attain a desired position
 54 anywhere in the domain of concern

55 Thus, navigation is inherently in real-time and depends on positioning; positioning depends
 56 on timing. We also suggest re-navigation and re-positioning as post-processed corollaries,
 57 which may include knowledge or processing capabilities not available *in situ*.

58 While RAFOS floats championed one-way ranging for re-positioning ([Duda et al., 2006](#);
 59 [Rossby et al., 1986](#)), the ability to do so for navigation was facilitated by the advent of the
 60 WHOI Micro-Modem ([Singh et al., 2006](#)) and synchronized clocks ([Rypkema et al., 2017](#)).

61 AUV navigation efforts have achieved root mean square (rms) localization error on the order
62 of tens of meters relative to GNSS surface position over less than ten kilometers in shallow
63 ([Claus et al., 2018](#); [Eustice et al., 2007](#); [Kepper et al., 2017](#)) and deep water ([Jakuba et al.,](#)
64 [2008](#); [Kunz et al., 2008](#); [Webster et al., 2009](#)). However, these efforts all used a nominal
65 sound speed for travel time conversion and the vehicles were limited to shallower isovelocity
66 regimes.

67 Localization algorithms that do consider environmental or acoustic uncertainty tend to
68 focus on longer duration and larger range experiments, where spatio-temporal variability
69 cannot be ignored. These methods have also been reserved for post-processing as they can
70 be labor intensive, computationally heavy, and/or require additional information like con-
71 temporaneous data. For example, measured basin scale acoustic arrivals on gliders equipped
72 with acoustic modems have been later unambiguously associated with predicted ray arrivals,
73 differing by 914 m rms from flight model positions, with an estimated uncertainty of 106
74 m rms ([Van Uffelen et al., 2013](#)). A follow up study investigated how accounting for glider
75 velocity between acoustic receptions could mitigate position error during a four-month glider
76 mission, but a single SSP was used ([Van Uffelen et al., 2016](#)). [Wu et al. \(2019\)](#), given three
77 days of real acoustic records, generate synthetic records through ocean model snapshots, and
78 cross correlate the two to estimate absolute range between a bottom-moored transmitter and
79 a bottom-moored receiver with 150 depths. While potentially applicable for various deep
80 ocean states, this is reliant on model realism and impractical for real-time operations. Lastly,
81 a “cold start” algorithm that does not require prior knowledge of track, position, or sound
82 speed information isolates the last path detected in a full multipath pattern ([Mikhalevsky](#)

83 *et al.*, 2020). Then, a representative group speed is solved for together with position in a
84 least squares fashion. This approach re-positioned a bottom-moored vertical hydrophone
85 array with an error of 58 m and a standard deviation of 32 m based on six sources 129–450
86 km away; accuracy can be improved by incorporating a four-dimensional sound speed field
87 from a general circulation model and this approach remains to be seen for navigation.

88 The ICEX20 AUV deployment necessitated an environmentally- and physically-driven
89 relationship between recorded travel times and estimated pseudoranges due to the multipath
90 uncertainty brought upon by an increasingly observed double-ducted environment in the
91 Beaufort Sea, which some refer to as the “Beaufort Lens” (Chen *et al.*, 2019; Chen and
92 Schmidt, 2020; Litvak, 2015).

93 Given that a lens introduces significant ray refraction, the Beaufort Lens is a shorthand for
94 the spatio-temporal variability of the local temperature and sound speed maxima generally
95 around 50 to 60 m in depth. A neutrally buoyant layer of warm Pacific Summer Water
96 creates a unique double-ducted environment —the upper duct degrades signal coherence
97 due to intensified ice interaction and the lower duct effectively traps sound for long range
98 propagation (Poulsen and Schmidt, 2017). Modeling output (Duda *et al.*, 2021, 2019) and
99 experimental observations (Ballard *et al.*, 2020; Bhatt, 2021) suggest that, in the Beaufort
100 Sea, the duct is persistent and widespread but not necessarily continuous; it and its acoustic
101 effects can be non-existent, minimal, or drastic. Transmissions in the upper duct, between
102 the surface ice and the lens, degrade in signal coherence with repeated reflections under
103 the ice. In the lower duct, between the lens and its conjugate depth in the Atlantic water

¹⁰⁴ (roughly 200 m), sound above 350 Hz is trapped near losslessly for long range propagation
¹⁰⁵ ([Poulsen and Schmidt, 2017](#)).

¹⁰⁶ The Arctic, while remote, is the perfect place to demonstrate mature navigation tech-
¹⁰⁷ nologies in real GNSS-denied conditions. Thorough reviews of uncrewed vehicle operations
¹⁰⁸ in polar environments can be found in [Norgren et al. \(2014\)](#) and [Barker et al. \(2020\)](#); there
¹⁰⁹ is no comparable work in the Arctic for a short range AUV deployment in the Beaufort
¹¹⁰ Lens. Seminal Arctic AUV deployments ([Bellingham et al., 1995](#); [Brooke, 1981](#); [Hayes and](#)
¹¹¹ [Morison, 2002](#); [Jackson, 1983](#); [Light and Morison, 1989](#)) and more recent ones ([Fossum](#)
¹¹² [et al., 2021](#); [Jakuba et al., 2008](#); [Kukulya et al., 2010](#); [Kunz et al., 2008](#); [Plueddemann et al.,](#)
¹¹³ [2012](#); [Timmermans and Winsor, 2013](#)) witnessed the classical upward refracting sound speed
¹¹⁴ profile that is amenable to an isovelocity assumption.

¹¹⁵ Of note, despite different platforms and scales, are recent glider deployments in the
¹¹⁶ Canada Basin. In 2014, in partially ice-covered conditions, a long range LBL system with
¹¹⁷ WHOI Micro-Modems at 100 m depth exploited the lower duct for long range communication
¹¹⁸ with two gliders ([Freitag et al., 2016](#); [Webster et al., 2015](#)). The sound speed value measured
¹¹⁹ at the time of reception was used to estimate pseudorange in post-processing. The beacon-
¹²⁰ to-beacon performance was excellent, achieving contact at ranges greater than 200 km with
¹²¹ a position uncertainty of 40 m. The beacon-to-glider performance, however, deteriorated
¹²² due to missed contacts outside the duct, and was not described quantitatively. In 2017,
¹²³ gliders were deployed in a region with no ice coverage ([Graupe et al., 2019](#)). Ranges were
¹²⁴ linearly scaled by a statistical description of SSPs taken during the experiment, 1450 ± 6.5
¹²⁵ m/s. This resulted in an error of 550 m, which was reduced by a factor between 4 and

126 5, depending on the dive, using a post-processing acoustic arrival matching method. Both
127 cases exploit the lower duct for high fidelity communication at long ranges. Unintuitively,
128 the smaller scale nature of our deployment during ICEX20 is not a simplifying factor. For
129 source depths typical to vehicle operations, 30 to 200 m, the Beaufort Lens introduces a
130 shadow zone that spans from 2 to 6 kilometers in range ([Schmidt and Schneider, 2016](#)).

131 Compared to previous small-scale navigation efforts, the approach in this paper integrates
132 real-time model-aided data processing to estimate a representative sound speed along a path
133 from source to receiver, leveraging climatology, *in situ* data, and fast acoustic modeling. The
134 paper is organized as follows. Section [II](#) details the experimental approach and conditions
135 during ICEX20. Given that there is no GNSS ground truth for the vehicle position while
136 underway, we first evaluate the real-time ranging performance of GNSS-linked beacon-to-
137 beacon communication events in section [III](#). Section [IV](#) uses insights from field data to
138 introduce a new ray filtering algorithm to improve range estimation. Section [V](#) emulates the
139 real-time processing pipeline to re-position beacon-to-beacon events and re-navigate AUV
140 *Macrura*.

¹⁴¹ **II. OVERVIEW OF THE ICEX20 EXPERIMENT**

¹⁴² The results from this paper derive from data collected while deploying the AUV *Macrura*,
¹⁴³ a custom Bluefin-21, during the Ice Exercise 2020 (ICEX20). The experiment was conducted
¹⁴⁴ in the Beaufort Sea, from March 8th to 11th, at roughly 71.2°N. The AUV deployment
¹⁴⁵ was supported by the Integrated Communication and Navigation Network (ICNN) ([Ran-](#)
¹⁴⁶ [deni et al., 2020](#); [Schneider et al., 2021](#)), a specialized implementation of the LBL solution.
¹⁴⁷ The ICNN was initially developed via numerous virtual experiments to ensure robust algo-
¹⁴⁸ rithms and interfaces between different hardware components. The simulation capabilities
¹⁴⁹ are largely physics-driven with a modular system of systems approach—an environmental
¹⁵⁰ simulator with sub-components for the ocean, including Arctic ice drift and ocean acoustic
¹⁵¹ propagation; a vehicle simulator with sub-components for vehicle dynamics and navigation;
¹⁵² a topside hardware simulator and acoustic communications simulator, both with a software-
¹⁵³ only configuration and a hardware-in-the-loop version ([Schneider and Schmidt, 2018](#)). The
¹⁵⁴ virtual environment similarly emulates the interfaces between the real components to test
¹⁵⁵ the entire software pipeline.

¹⁵⁶ **A. The Integrated Communication and Navigation Network**

¹⁵⁷ The ICNN is comprised of four ice buoys in a loose rectangle, roughly 2 km away from
¹⁵⁸ a central ice camp with a topside computer, as shown in Fig. 1. Each ice buoy is outfitted
¹⁵⁹ with a Garmin GPS 18x, with a pulse-per-second rising edge aligned to 1 microsecond and
¹⁶⁰ a specified accuracy of 3 m, 95% of the time. They are also each equipped with a WHOI

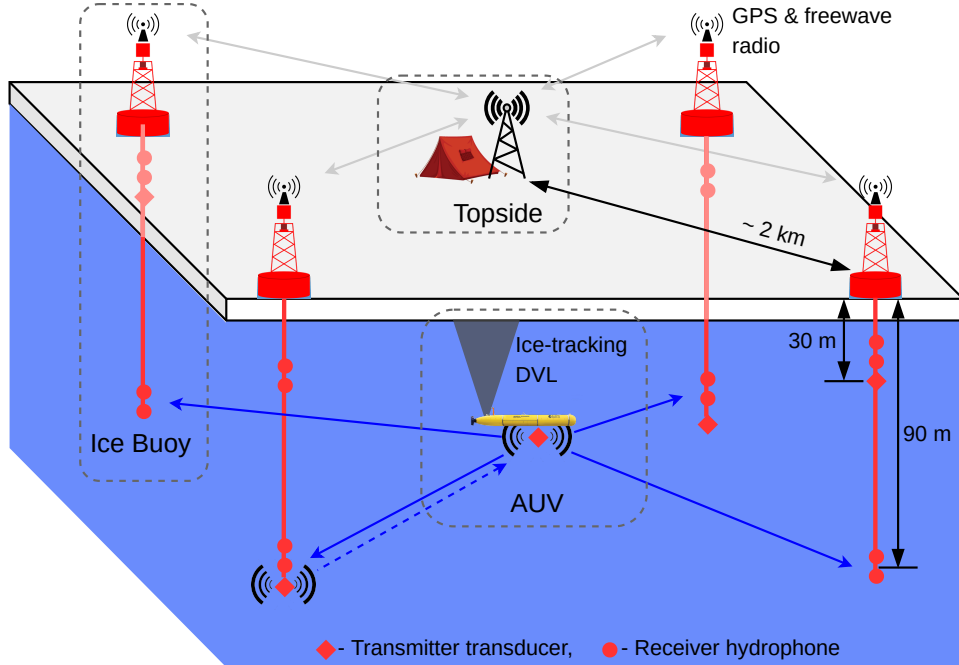


FIG. 1. A schematic overview of the Integrated Communication and Navigation Network (ICNN), which provides joint data transfer and tracking between an AUV and a human decision maker at the topside camp.

161 Micro-Modem ([Gallimore et al., 2010](#); [Singh et al., 2006](#)), with a four-element receiver array,
 162 a single transmitter, and a real-time clock featuring a precision of 2 ppm and a resolution of
 163 one-tenth of a millisecond. Acoustic messages were sent with a 10 kHz carrier frequency, 5
 164 kHz bandwidth, and phase-shift keying (PSK) modulation on a time-division multiple access
 165 schedule with a thirty-second cycle, giving room for two-way communication throughout the
 166 operational volume. Thus the ICNN is dependent on the successful decoding of acoustic
 167 transmissions. The receive and transmit elements were split between shallow and deeper
 168 depths—30 and 90 m—to provide better coverage across the shadow zone. While each buoy
 169 only has one transmit depth, all buoys have both receive depths but the depth of the active

170 receive layer is synchronized across all buoys. The design of the ICNN enables a self-adapting
171 network to transmit and receive at the optimal depth to maintain contact with the AUV
172 (Schneider *et al.*, 2021). The buoys do not encompass the full horizontal range of the vehicle
173 but are positioned to minimize overlap in trilateration for spherical positioning (Deffenbaugh
174 *et al.*, 1996a).

175 To balance competing uses of the acoustic channel, the network uses a single synchronized
176 digital communication packet to provide both tracking and data to the operator.

177 1. The AUV, running an ice-tracking doppler velocity log (DVL) and an onboard hydro-
178 dynamic model, broadcasts its perceived location on a scheduled, time-synchronized
179 message via WHOI Micro-Modem

180 2. Four ice buoys, each outfitted with a WHOI Micro-Modem, receive messages from the
181 AUV and send that information over freewave radio to a topside computer

182 3. The topside computer converts travel times into pseudorange estimates using a stochas-
183 tic embedded prediction of the effective horizontal sound speed via BELLHOP ray
184 tracing code (Porter, 2011) using a sound speed profile provided by an updatable
185 Virtual Ocean (Bhatt *et al.*, 2022; Schneider and Schmidt, 2018)

186 4. The topside computer calculates a new position by trilaterating the range estimates

187 5. To combat latency and intermittency, the position differential, not the absolute po-
188 sition, is broadcast from a 20 m source at topside to update the vehicle’s navigation
189 solution

190 The AUV *Macrura* was deployed through a hydrohole from an ice camp but recovered
 191 through an emergency hydrohole, as shown in Fig. 2. A random disk error stalled *Macrura*
 192 underneath the ice but did not prevent it from transmitting its location. An exploratory
 193 hole at *Macrura*'s self-reported position confirmed its presence. Due to an incoming storm,
 194 the vehicle was tied off to a physical marker on the ice, and three days later, *Macrura* was
 195 recovered. The ice camp had moved roughly 19 km and the AUV's relative position to
 196 camp had also changed, from roughly 45°at 1000 m to 90°at 1100 m. While the emergency
 197 recovery serves as qualitative proof of navigation, this paper specifically addresses the third
 198 and fourth steps—the conversion of travel times into pseudoranges and its quantitative effect
 199 on trilateration. By focusing on pseudorange estimates between GNSS-tracked beacons, and
 200 re-running the trilateration pipeline, the results are decoupled from all other mechanisms in
 201 the ICNN.

202 B. ICEX20 sound speed conditions

203 An important component to the navigation solution is an accurate estimation of a rep-
 204 resentative SSP for the ocean volume. Previous field experience, during Ice Exercise 2016
 205 (ICEX16), demonstrated the negative effects of the Beaufort Lens on tracking and commu-
 206 nication ([Schmidt and Schneider, 2016](#)). Fig. 3 shows historical, modeled, and *in situ* sound
 207 speed data for both ICEX16 and ICEX20. These three input streams were selected to mirror
 208 the information available on a submarine (personal conversation with LT B. Howard and LT
 209 CDR D. Goodwin). In the field, the SSP information was shared with the vehicle via basis
 210 representation compression on a lightweight digital acoustic message ([Bhatt et al., 2022](#)).

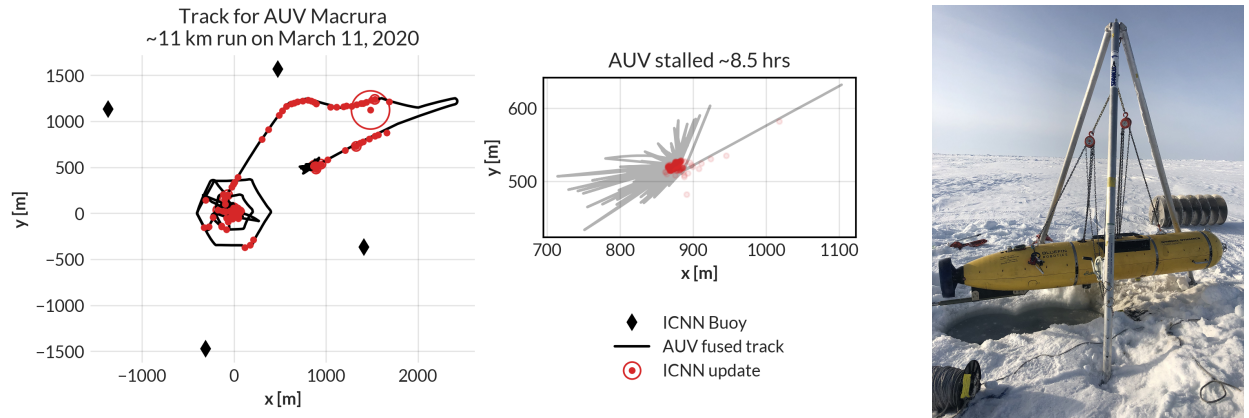


FIG. 2. The under-ice mission track for AUV *Macrura* (left), including the position updates as it stalled underneath the ice overnight (middle). A marker was placed on the ice at the vehicle's estimated self-location. It was recovered after a three day storm within a meter of the marker (right).

211 All modeled data comes from the Hybrid Coordinate Ocean Model (HYCOM) ([Chassagnet](#)
 212 *et al.*, 2007), which does not seem to capture the forcing mechanisms that cause the Beaufort
 213 Lens. For ICEX16, the data-driven profile was sourced from nearby Ice Tethered Profilers
 214 (ITP) after the field experiment ([Krishfield et al.](#), 2008; [Toole et al.](#), 2011) and exhibits a
 215 fairly deep lens; the historical profile is from the World Ocean Atlas ([National Centers for](#)
 216 [Environmental Information](#), 2013). For ICEX20, the chosen weights (data-driven) profile
 217 derives from initial CTD casts taken on site, showing an intense warm water intrusion; the
 218 baseline (historical) profile, showing moderate ducted conditions, comes from the average
 219 of March 2013 ITP data. This month best matched sea ice and sound speed conditions
 220 at the beginning of ICEX20 ([Bhatt et al.](#), 2022). It is important to note that all profiles
 221 that do show the Beaufort Lens do so with different local sound speed maxima at different

²²² depths, reflective of the wide range of lens properties observed for all ITP data in the region.
²²³ The variability of the lens height and prominence is the main reason an updatable SSP was
²²⁴ integrated into the ICNN solution.

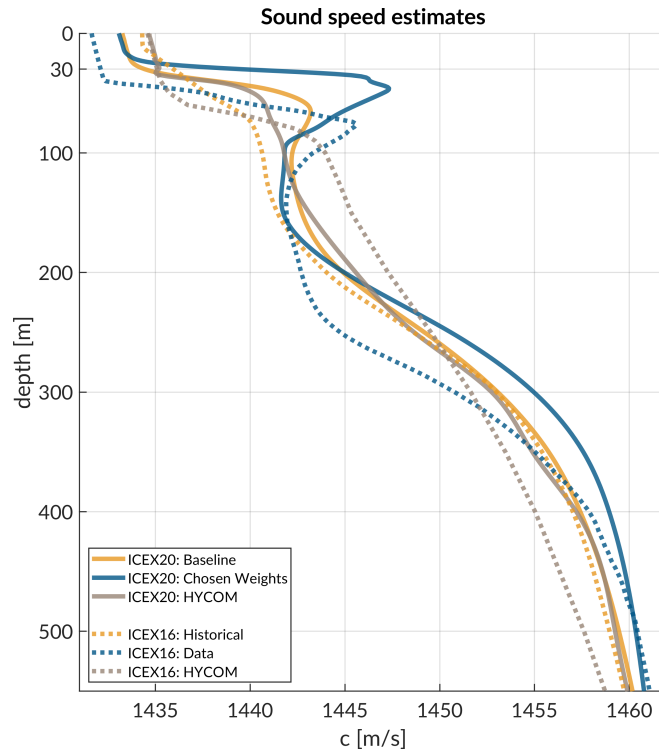


FIG. 3. Sound speed profiles for historical (baseline), data (chosen weights), and HYCOM model for both ICEX16 and ICEX20.

²²⁵ During ICEX20, the HYCOM profile was available but never deployed. For post-
²²⁶ processing comparison, we introduce both the HYCOM profile and an isovelocity case,
²²⁷ 1441.8 ± 3.7 m/s, as the mean and standard deviation of the observed sound speed profile
²²⁸ over the first 200 m. This is a contrived value taken in the style of [Graupe et al. \(2019\)](#)
²²⁹ for the sake of comparison; the default value in the ICNN, which was not environmentally
²³⁰ informed and used when no updates were available, was 1430 m/s.

231 **III. REAL-TIME PSEUDORANGE ANALYSIS**

232 Because the vehicle’s navigation solution during a mission can only be evaluated on the
233 basis of the error estimates sent, a separate experiment for validating the real-time ranging
234 approach was conducted. Ice buoy modems were run as “virtual vehicles” at a fixed depth,
235 receiving position updates from the other beacons as well as from a camp site modem lowered
236 to 20 m. Fig. 4 shows successful events sorted by source depth. In this analysis, we assume
237 there is insignificant displacement between the GNSS puck surface expression and subsurface
238 modem; this is supported by unusually low observed ice drift rates, just 0.7 cm/s on average
239 throughout the mission.

240 **A. Minimal bounce (MB) criteria**

241 The fundamental challenge to implement GNSS-like navigation, especially in an acousti-
242 cally complex propagation environment, is characterizing a single sound speed to compensate
243 for the effects of ray refraction and reflection. The use of the acoustic modem network for
244 tracking relies on the accurate estimation of travel times between the submerged platform
245 and LBL beacons, supported by clock synchronization and a pre-determined scheduling of
246 acoustic events. For the Beaufort Lens in particular, the strong multipath effects make it
247 virtually impossible to deterministically predict the modem’s detected arrival time.

248 Instead, for each individual receiver i , an embedded stochastic tracking framework is used
249 to provide a running estimate of the effective sound speed $c_{i,j}$ for the conversion from travel
250 time to range from modem j , with the ultimate goal of matching the implied horizontal

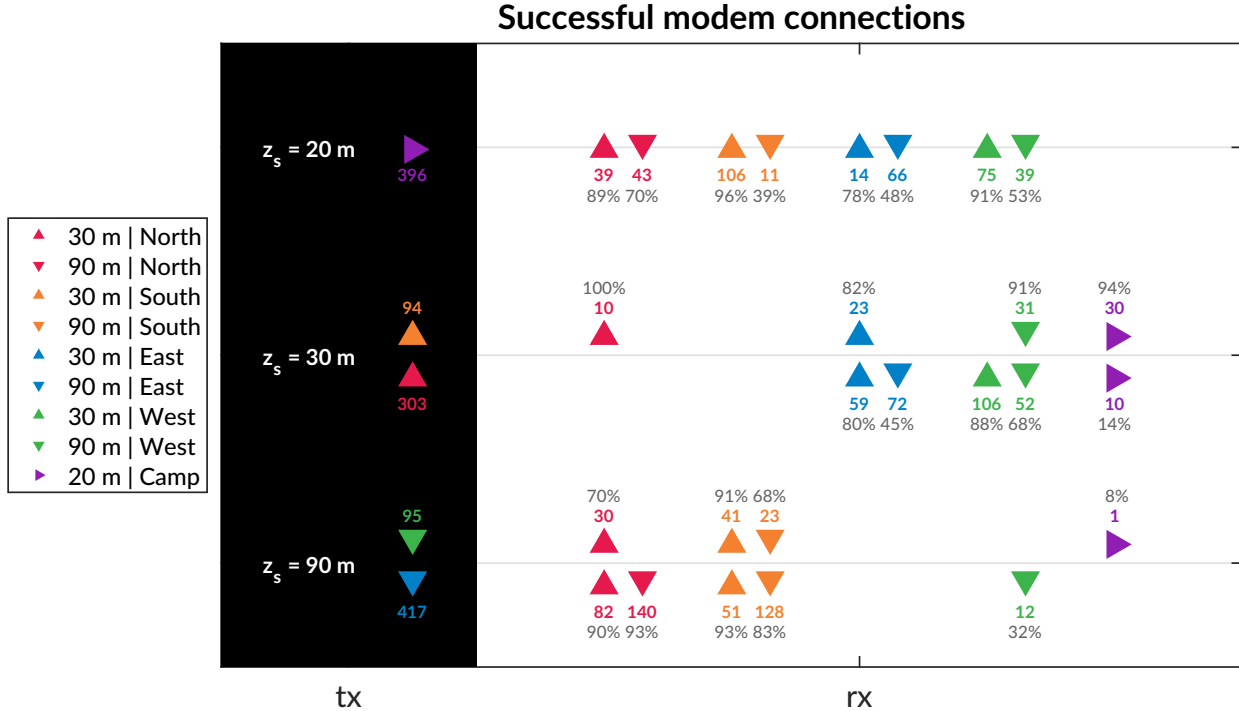


FIG. 4. An overview of the modem experiment by source and receiver depth and position. The black column on the left, *tx*, shows the source depth, z_s , with the total number of transmissions. The column on the right, *rx*, shows the receivers with the number of successful decodings and the percent success rate, defined as the ratio of decoded to detected. The orientation of the triangles—sideways, upwards, and downwards—corresponds to depths of 20, 30, and 90 m.

251 effective sound speed, i.e., the GNSS-recorded distance between two nodes divided by the
 252 modem-recorded OWTT between them.

253 In the ICEX20 configuration, the acoustic tracker is running on the topside computer,
 254 which controls the ICNN. Here we assume that the effective sound speeds $c_{i,j}$ are smoothly

255 varying over the course of a vehicle mission, i.e., with respect to range from signal origin at
 256 transmitter j , mission time, and the thirty-second interval between transmissions.

257 When the topside tracking framework receives a message, with a time delay, Δt , it re-
 258 quests a new estimate for $c_{i,j}$ and its standard deviation. The effective sound speed is
 259 computed using the vehicle's reported depth and the extrapolated navigation solution for
 260 range, \hat{r} , as inputs to the ray tracing program, which returns an impulse response estimate
 261 in the form of ray travel times dt_j and amplitudes a_j .

262 The initial call to BELLHOP is over a local grid centered at the range and depth posited
 263 by the onboard tracking solution. The grid, compared to a point solver, adds redundancy
 264 in resolving the actual multipath structure for a reliable acoustic path without overtaxing
 265 onboard computational time and memory. It is initialized as 11×11 points spanning 10 m
 266 horizontally and 20 m vertically. The horizontal dimension reflects the accumulated vehicle
 267 position error given a thirty-second communication cycle; the vertical dimension reflects
 268 how, computationally, eigenrays of the same time front seem to stack vertically in the water
 269 column. For each grid point, BELLHOP produces several arrivals resulting from multiple
 270 propagation paths. Using only the N_0 rays with neither surface nor bottom bounces, the
 271 tracking system will then estimate the current effective sound speed c from a power weighted
 272 average of the ray travel times,

$$c = \frac{\hat{r} \sum_{n=1}^{N_0} a_n^2}{\sum_{n=1}^{N_0} dt_n a_n^2}, \quad (1)$$

273 and the associated weighted standard deviation,

$$\sigma_c \simeq \sqrt{\frac{\sum_{n=1}^{N_0} (dt_n - \hat{r}/c)^2 a_n^2}{\sum_{n=1}^{N_0} a_n^2}} \frac{c^2}{\hat{r}} \quad (2)$$

²⁷⁴ If no direct paths exist, i.e. $N_0 = 0$, then the effective speed is computed using the same
²⁷⁵ algorithm for the ray arrivals with one bounce, and so on.

²⁷⁶ Finally, the pseudorange is calculated simply as

$$r_{i,j} = c_{i,j} \Delta t_{i,j} \quad (3)$$

²⁷⁷ Thus the minimal bounce (MB) criteria assumes the signal detected by the modem will be
²⁷⁸ dominated by a set of paths with the least number of boundary interactions. Importantly,
²⁷⁹ this stochastic, ensemble method for effective sound speed calculation is automated and
²⁸⁰ computationally lightweight for real-time use. The BELLHOP simulation that runs this cal-
²⁸¹ culation uses 3600 rays with launch angle fan of -60° to 60°, a representative depth-dependent
²⁸² sound speed profile, and a range-dependent bathymetry.

²⁸³ B. Pseudorange error metrics

²⁸⁴ The modem experiment generated 811 beacon-to-beacon communication events with ef-
²⁸⁵ fective sound speed predictions from a real-time MB implementation. Given the complexity
²⁸⁶ of the ICNN system, this experiment did not collect an exhaustive set of data across all
²⁸⁷ buoy, source depth, receive depth, and model sound speed combinations.

²⁸⁸ Fig. 5 shows the range error boundary for both SSP inputs used in ICEX20. The
²⁸⁹ algorithm generally overestimates pseudoranges because it resolves the effective sound speed
²⁹⁰ for the most direct path. The baseline SSP (n=243 events) has an absolute pseudorange
²⁹¹ error of 11.38 ± 4.23 m; the weighted SSP (n=568), 11.36 ± 8.12 m. The discrepancy
²⁹² between these two is largely due to outlier events only contained in the weighted SSP set.

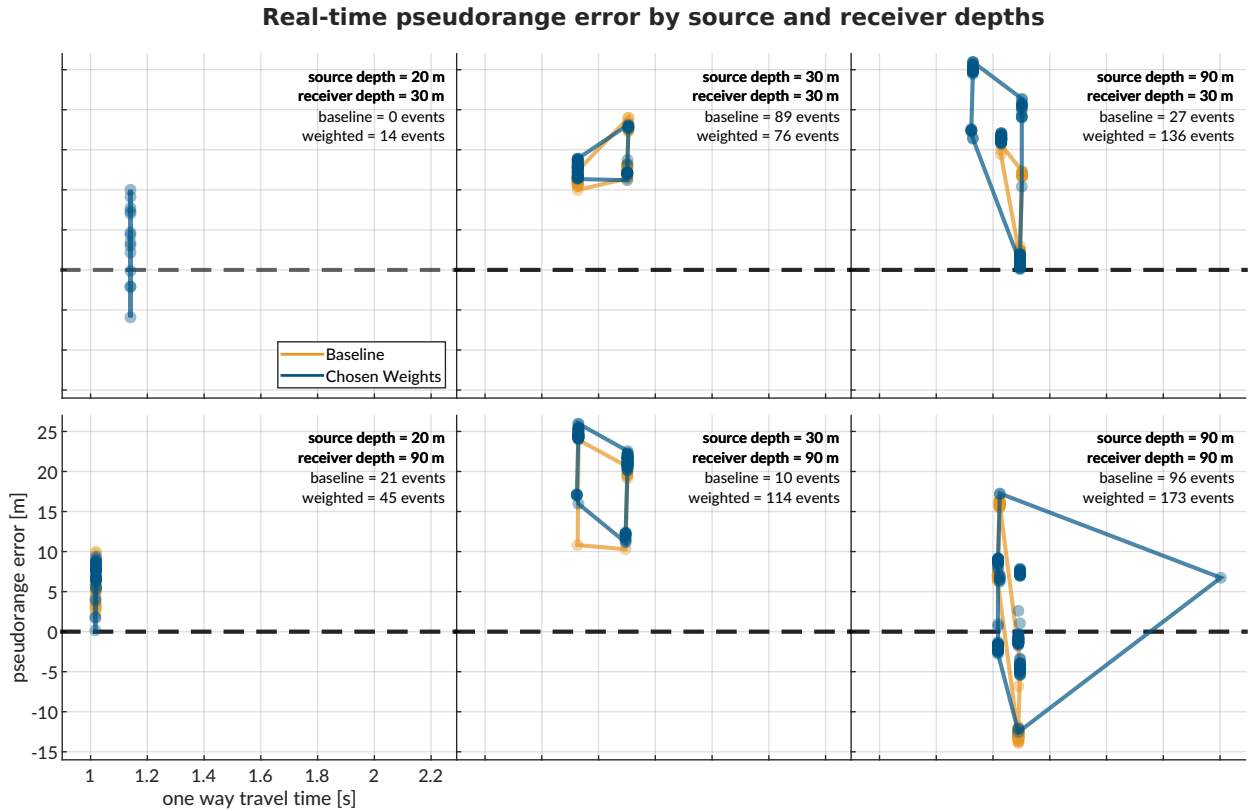


FIG. 5. The real-time range pseudorange error relative to GNSS-derived range by source (columns: 20, 30, and 90 m) and receiver (rows: 30 and 90 m) pairings for both sound speed estimates used during ICEX20. The number of transmissions is noted in the top right of each panel under the source and receiver depths. The dashed line indicates no range error, and the boundary drawn indicates scope of the range error as a function of one-way travel time.

293 Where there is overlap between sound speed conditions used for the real-time MB approach,
 294 the pseudorange error difference is no more than a few meters. The overarching results
 295 show that sound speed estimates derived from eigenrays for a local grid, as opposed to a
 296 singular point, are accurate enough to support vehicle navigation. A promising sign that
 297 the MB method adapts sound speed somewhat intelligently is the lack of error growth as
 298 travel time increases. While the MB looks for just the least complex multipath, the high

²⁹⁹ density of launch angles almost always guarantees a direct path for the beacon-to-beacon
³⁰⁰ configurations. Nonetheless, the consistent overestimation of pseudorange invites further
³⁰¹ analysis into acoustic arrival matching.

³⁰² **C. Eigenray identification for beacon-to-beacon events**

³⁰³

³⁰⁴ Accounting for ice movement between beacons creates nominal ranges with small vari-
³⁰⁵ ability. Figs. 6, 7, and 8 show eigenrays for three SSPs, for source depths of 20, 30, and 90
³⁰⁶ m, respectively. Eigenrays were initially found using the built-in BELLHOP protocol with
³⁰⁷ a launch angle fan of 2400 rays between -60° and 60°. Separately, recorded travel times be-
³⁰⁸ tween beacons were clustered with 1 millisecond boundaries such that some source-receiver
³⁰⁹ pairs had multiple distinct travel times. The BELLHOP eigenray returns were then filtered
³¹⁰ such that one was selected per travel time cluster per SSP; bottom bounces were recovered
³¹¹ but filtered out. The three source depths create distinct ray geometries with respect to the
³¹² three sound speed inputs.

³¹³ **1. Source depth of 20 m**

³¹⁴ For a source at 20 m depth, shown in Fig. 6, reliable eigenrays are found for all sound
³¹⁵ speed inputs. Rays refract upwards and intersect with the shallow and deep receiver locations
³¹⁶ between 1.5 and 1.8 km in range. However, the ray paths for the shallow receivers change
³¹⁷ both in the number of surface interactions and where the surface interactions occur with
³¹⁸ respect to range across the SSPs. As the Beaufort Lens strengthens, the chosen paths to

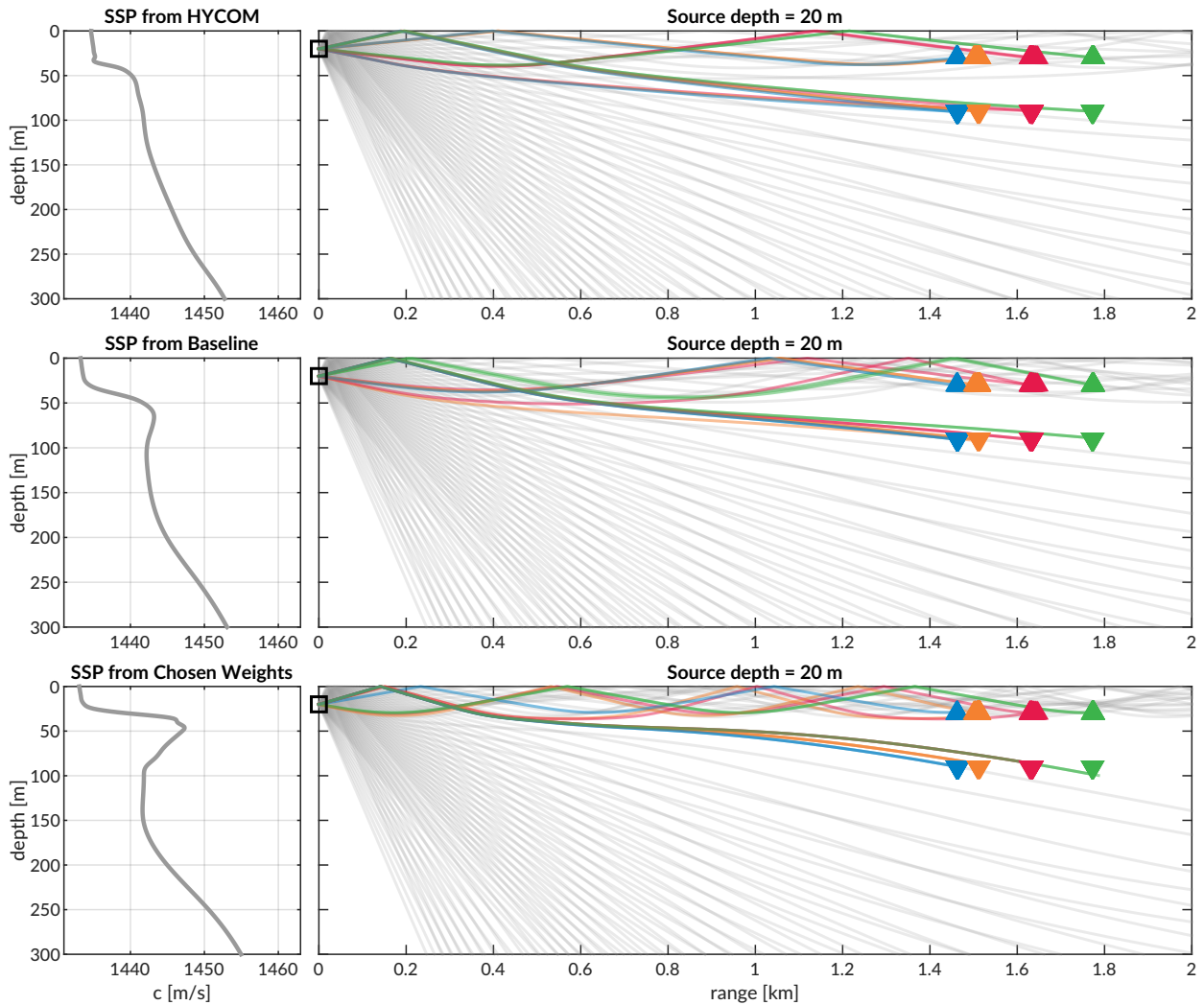


FIG. 6. Eigenrays for beacon-to-beacon events for each sound speed with a nominal source depth of 20 m over a total ray fan in gray. The Beaufort Lens strengthens from HYCOM to baseline to chosen weights SSP. The beacons are highlighted in the color/marker encoding from Fig. 4.

319 the second farthest shallow buoy (North, in red) interact with the surface more and become
 320 distinct. The weighted SSP shows the most interesting effects for the deeper receivers. The
 321 ray paths all interact with the surface, and the eigenrays for the Northern (red) and Western
 322 (green) buoys are in fact the same ray.

323 2. Source depth of 30 m

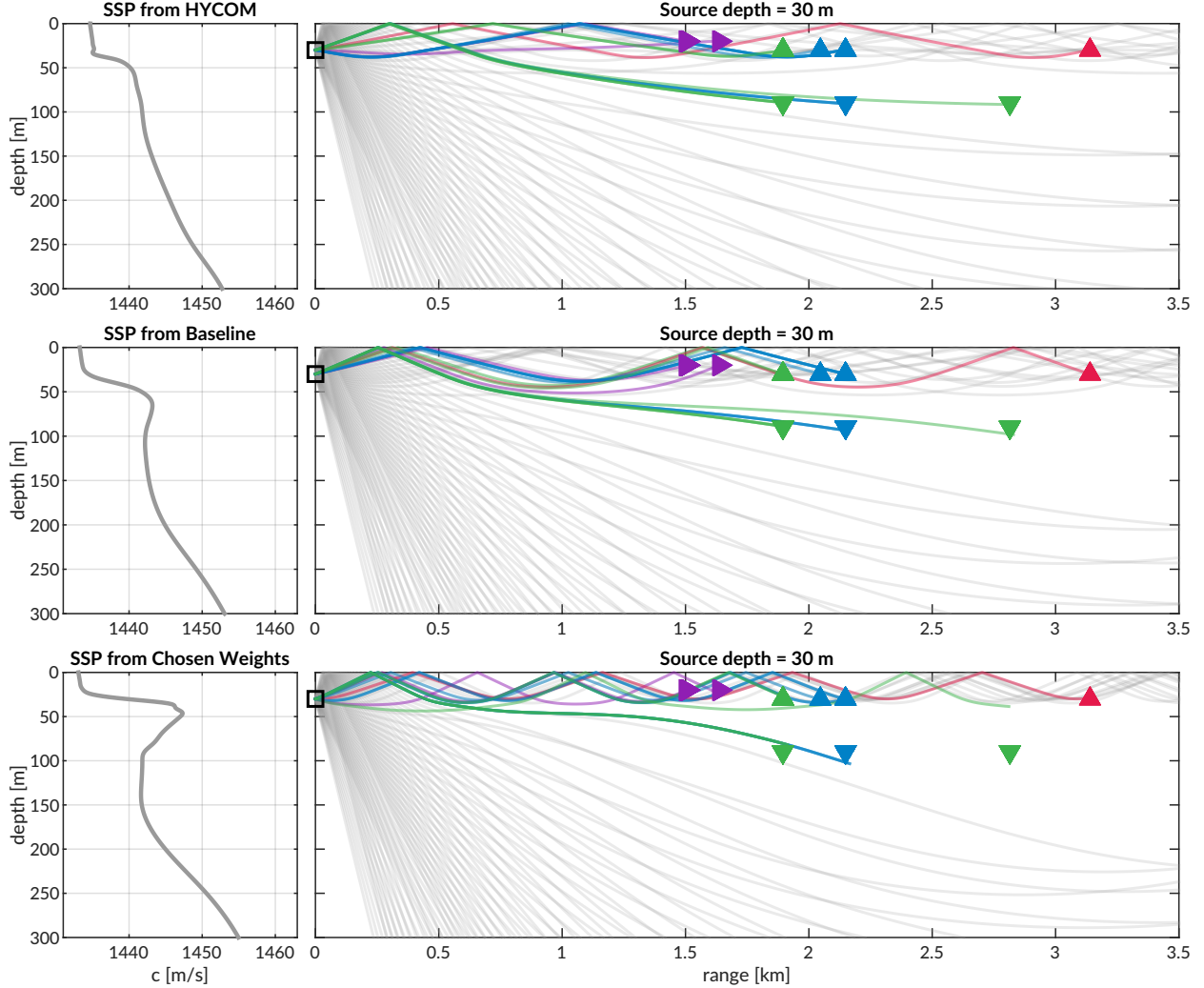


FIG. 7. Same as Fig. 6 except for a nominal source depth of 30 m.

324 The ray geometries from the 30 m source, in Fig. 7, show increased ducting and a corre-
 325 sponding degradation of eigenray identification. Receptions span 1.5 to 3.2 km. Eigenrays
 326 for HYCOM and the baseline SSP intersect with both shallow and deep receivers. Eigenrays
 327 for the weighted SSP show how the surface channel intensifies ice interactions for shallow
 328 receivers and how the shadow zone denies reliable acoustic paths to the deeper receivers.

329 The increasing number of surface reflections to the farthest shallow buoy (North, in red)
 330 demonstrates the MB criteria's tendency for overestimation. For the HYCOM, baseline,
 331 and weighted SSP inputs, the most appropriate eigenrays show two, three, and four surface
 332 interactions.

333 **3. Source depth of 90 m**

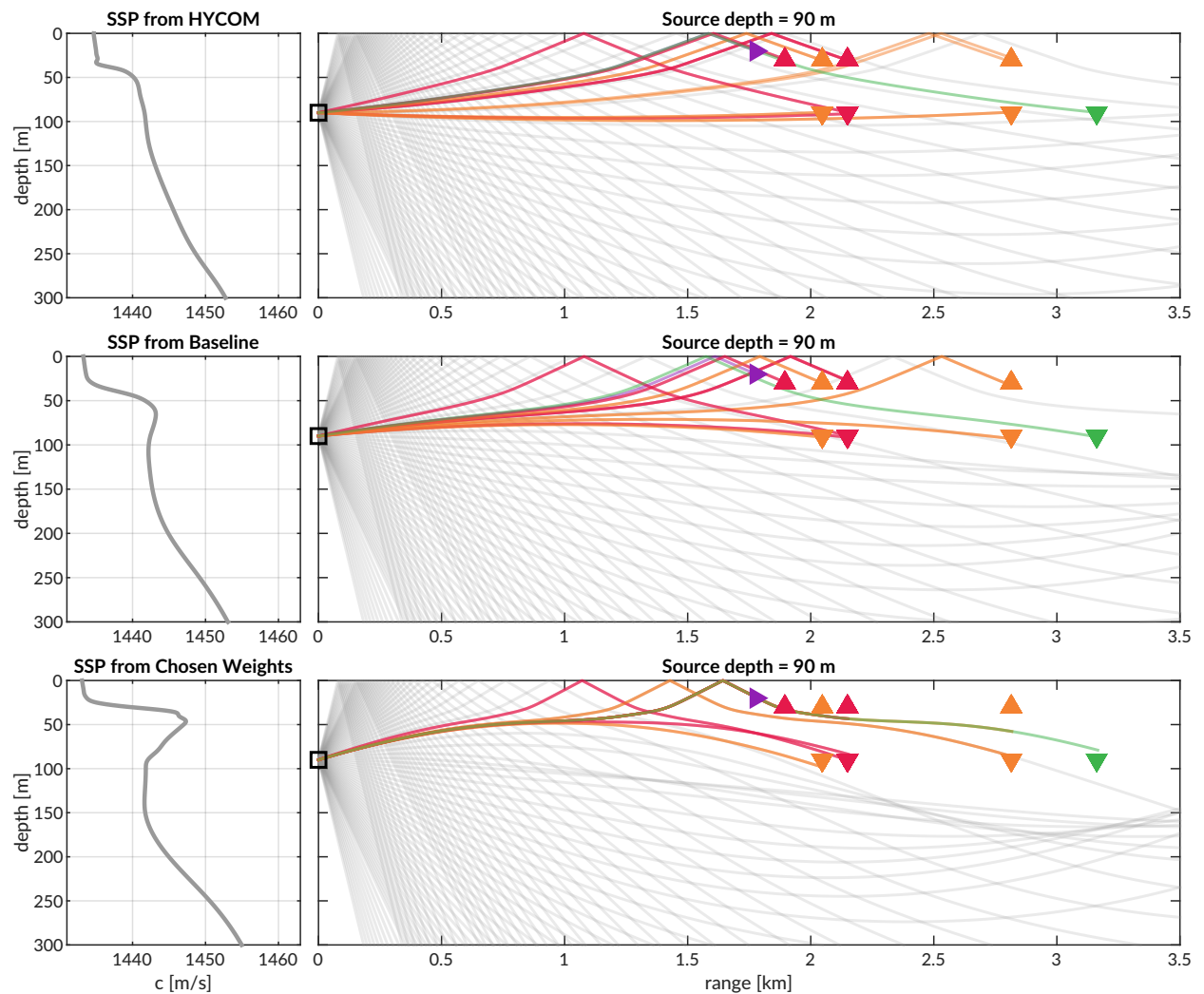


FIG. 8. Same as Fig. 6 except for a nominal source depth of 90 m.

334 Lastly, Fig. 8 shows ray geometries from the 90 m source, uncovering a different shadow
335 zone extent. While the receiver locations are similar to those from the 30 m source depth,
336 the deeper source depth effectively negates the upper duct and places the upper (and some
337 of the lower) receivers in unreliable acoustic paths. The HYCOM eigenrays show the most
338 reliable acoustic paths, but these deteriorate with increasing ducted conditions. The lack of
339 direct paths for the observed SSP further points out the shortcomings of the MB approach.

340 The goal of the MB algorithm was to provide a reliable, physically intuitive interpreta-
341 tion of the acoustic propagation, capturing the information provided by the acoustic model
342 without taking on the additional burden of identifying specific eigenrays that may connect
343 any given source-receiver pair. The MB algorithm exploited the effect of source and receiver
344 depth in the acoustic model, and its performance was sufficiently adequate for vehicle nav-
345 igation. However, the algorithm assumes that the most likely detected arrival is the most
346 direct path modeled, which was not generally the case under the observed ducted conditions.

³⁴⁷ **IV. POST-PROCESSED PSEUDORANGE ANALYSIS**

³⁴⁸ From all events recorded during the modem test experiment, there are 1,242 successfully
³⁴⁹ decoded beacon-to-beacon events. Thus, a post-processing analysis that emulates the real-
³⁵⁰ time navigation engine was run to overcome the unequal distribution of communication
³⁵¹ events with respect to depth, range, and sound speed status.

³⁵² It is important to note that the value for the extrapolated range, \hat{r} , is only tracked by
³⁵³ topside for a modem claiming to be the vehicle. In this section, \hat{r} is replaced with the GNSS-
³⁵⁴ tracked range for all modem events. The analysis therefore seeds realistic but “omniscient”
³⁵⁵ knowledge of the extrapolated range and emulates the post-processing pipeline to more
³⁵⁶ thoroughly evaluate the acoustic pseudorange estimate for all modem events. Sound speed
³⁵⁷ inputs are the isovelocity sound speed in addition to the ICEX20 modeled, baseline, and
³⁵⁸ weighted SSPs from Fig. 3. The analysis replicates the MB criteria but also introduces a new
³⁵⁹ filtering algorithm, the nearest bounce (NB), based on insights gleaned from the eigenray
³⁶⁰ analysis. Accordingly, the results in this section evaluate the utility of the algorithms and
³⁶¹ SSP sources, divorced from their role in the ICNN while maintaining relevance for real-time
³⁶² computation.

³⁶³ **A. Nearest bounce (NB) criteria**

³⁶⁴ The extent of ray bending and repeated reflections is dependent on the observed Beaufort
³⁶⁵ Lens. Based on this insight, a new algorithm, the nearest bounce (NB) criteria, is a slight
³⁶⁶ modification from the MB and includes multipath as a new dimension of information to

³⁶⁷ exploit. This metric, while run in post-processing, adds a negligible amount of computation
³⁶⁸ for real-time efficacy.

³⁶⁹ Given a running estimate for the effective sound speed $c_{i,j}$ between nodes i and j , the
³⁷⁰ navigation system has an extrapolated value for range, \hat{r} , and a recorded travel time, $\Delta t_{i,j}$.
³⁷¹ Instead of using only the N_0 rays with neither surface nor bottom bounces to estimate
³⁷² effective sound speed and iterating on additional bounces only if no valid direct path solutions
³⁷³ exist, we solve for the power-weighted average of the ray travel time for the N_k rays with k
³⁷⁴ bounces,

$$t_k = \frac{\sum_{n=1}^{N_k} dt_n a_n^2}{\sum_{n=1}^{N_k} a_n^2}, \quad (4)$$

³⁷⁵ find the nearest matching power weighted average to recorded travel time,

$$t_{i,j,k} = \min_{k=0,1,2,\dots} |t_k - \Delta t_{i,j}| \quad (5)$$

³⁷⁶ compute an effective sound speed,

$$c_{i,j} = \frac{\hat{r}}{t_{i,j,k}} \quad (6)$$

³⁷⁷ and estimate the range as was done previously.

$$r_{i,j} = c_{i,j} \Delta t_{i,j} \quad (7)$$

³⁷⁸ Whereas the MB outputs a scalar, this method first outputs a vector of effective sound
³⁷⁹ speeds based on the number of reflections. Then a single value is selected in a nearest-
³⁸⁰ neighbor fashion that best matches the recorded travel time, as the detected arrival is not
³⁸¹ always the first arrival or the direct path and could even be masked by noise or blocked
³⁸² temporarily (Deffenbaugh *et al.*, 1996b). The number of bounces is limited to four because

³⁸³ of the small operational scale and the attenuation accrued with many surface interactions.
³⁸⁴ Bottom bounces are not encoded separately because the ray paths refract upward, not due
³⁸⁵ to information limitations.

³⁸⁶ **B. Effective sound speed predictions**

³⁸⁷ The minimal and nearest bounce algorithms are applied with the three sound speed inputs
³⁸⁸ shown in Figs. 6, 7, 8. The resulting predicted effective sound speeds are shown in Fig. 9
³⁸⁹ for all source depths versus one-way travel time.

³⁹⁰ The goal of the effective sound speed prediction is to converge towards the implied sound
³⁹¹ speed, i.e., the GNSS-derived range divided by the recorded OWTT. As the environmental
³⁹² and ray filtering method become better representations of the real ocean, the lower the
³⁹³ expected mismatch is between the implied and estimated effective sound speeds.

³⁹⁴ The various sound speed inputs—isovelocity aside—not only modify the predicted effec-
³⁹⁵ tive sound speed, as seen by the colored vertical offsets, but often classify a distinct number
³⁹⁶ of bounces. HYCOM SSP fosters the most direct and one bounce multipath structures, lend-
³⁹⁷ ing a bias for faster speeds; the weighted SSP fosters the most double and triple bounces,
³⁹⁸ favoring slower speeds; the baseline SSP exists in between. Very rarely is the multipath
³⁹⁹ structure classified as a direct path, i.e., where the NB defaults to the MB prediction. In
⁴⁰⁰ fact, the higher the multipath classification, the more accurate the sound speed prediction
⁴⁰¹ is, likely driven by a tighter (or smaller) bundle of rays. Discontinuities in multipath clas-
⁴⁰² sification provide initial evidence for its importance to a smoothly varying effective sound
⁴⁰³ speed, as shown in the cluster of 30 to 30 m transmissions in Fig. 9, where HYCOM results

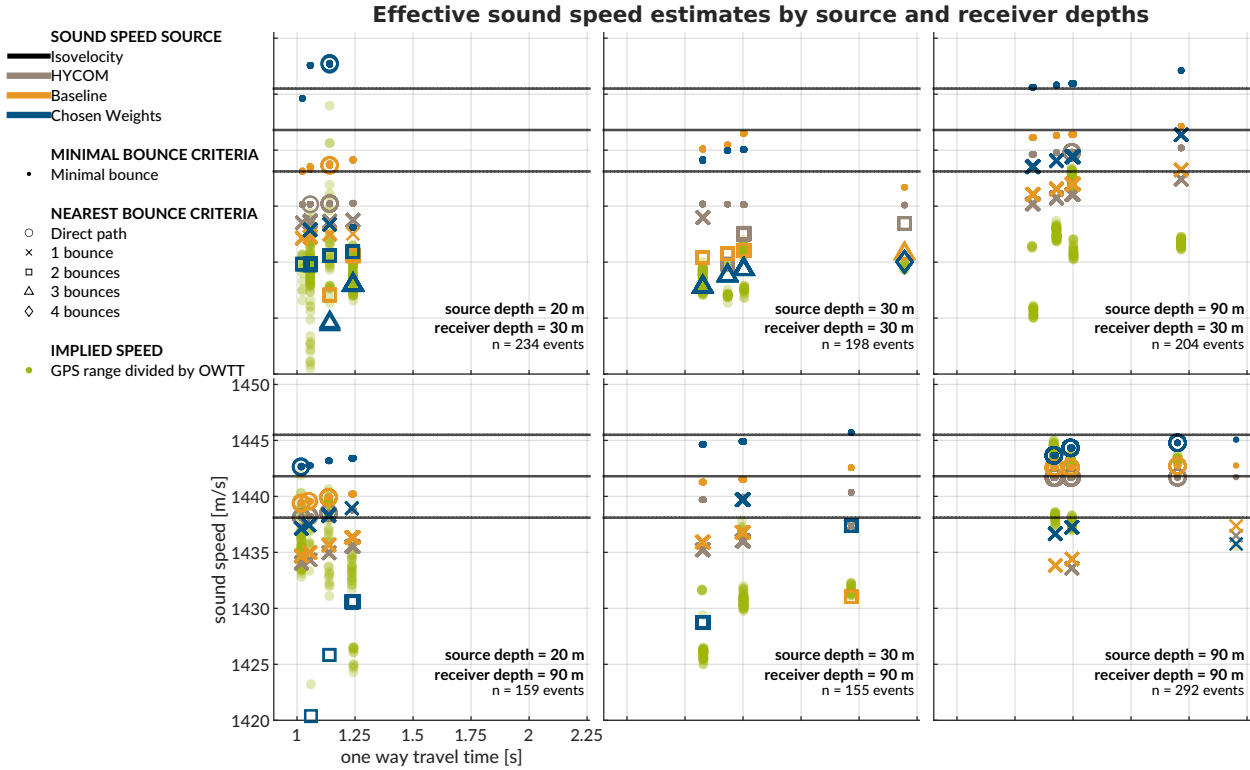


FIG. 9. A post-processing comparison of effective sound speed predictions for all beacon-to-beacon events. The rows share receiver depth; the columns share source depth. The recorded travel time is on the x-axis and the predicted effective sound speed is on the y-axis. The sound speed source is indicated by color and the isovelocity case is shown as the mean \pm the standard deviation. The effective sound speed using the minimal and nearest bounce criterion are distinguished by different marker shapes, compared to the separately colored green dots showing that from the implied calculation.

⁴⁰⁴ jump from one to two classified bounces while the baseline SSP and weighted SSP results
⁴⁰⁵ smoothly increase and exhibit two and three classified bounces, respectively. Of course, the
⁴⁰⁶ prediction deteriorates with cross-layer transmissions across the duct, but not to the same
⁴⁰⁷ degree at which eigenrays could not be found for the weighted SSP in section III C. The

⁴⁰⁸ evidence suggests that the grid based method provides a useful amount of redundancy to
⁴⁰⁹ resolve similar enough eigenrays.

⁴¹⁰ It is useful to think about in what case the isovelocity—or any isovelocity framing—would
⁴¹¹ have been appropriate. The transmissions from shallow to shallow receiver may have
⁴¹² matched the default configuration of 1430 m/s. The isovelocity contrived for this paper,
⁴¹³ 1441.8 m/s, best matches the transmissions from 90 to 90 m. Over the course of the four
⁴¹⁴ day experiment, the local maxima of the Beaufort Lens changed from roughly 1447 m/s
⁴¹⁵ at 40 m to 1442 m/s at 60 m. Given that implied sound speeds just for beacon-to-beacon
⁴¹⁶ events span 1420 to 1445 m/s, it is safe to say that a nominal sound speed would sacrifice
⁴¹⁷ pseudorange accuracy somewhere, and that an adaptive approach is necessary even for short
⁴¹⁸ duration and/or small-scale operations.

⁴¹⁹ C. Pseudorange error metrics

⁴²⁰ Pseudorange estimation plays an important role in trilateration. Fig. 10 shows the
⁴²¹ directional pseudorange error “footprints” for the four sound speed inputs with the NB
⁴²² approach, separated by source and receiver depth configurations.

⁴²³ The weighted SSP range error generally has the smallest and most zero-centered footprint
⁴²⁴ compared to HYCOM or baseline SSP, except for cross-layer source-receiver pairings between
⁴²⁵ 30 and 90 m in depth. The increased error for these is most likely driven by the computational
⁴²⁶ artifacts encountered by propagating through or near the shadow zone (see Fig. 7). In
⁴²⁷ comparison, source-receiver pairings between 20 and 90 m in depth are closer in range and
⁴²⁸ just outside or on the edge of the shadow zone (see Fig. 6), such that the corresponding ray

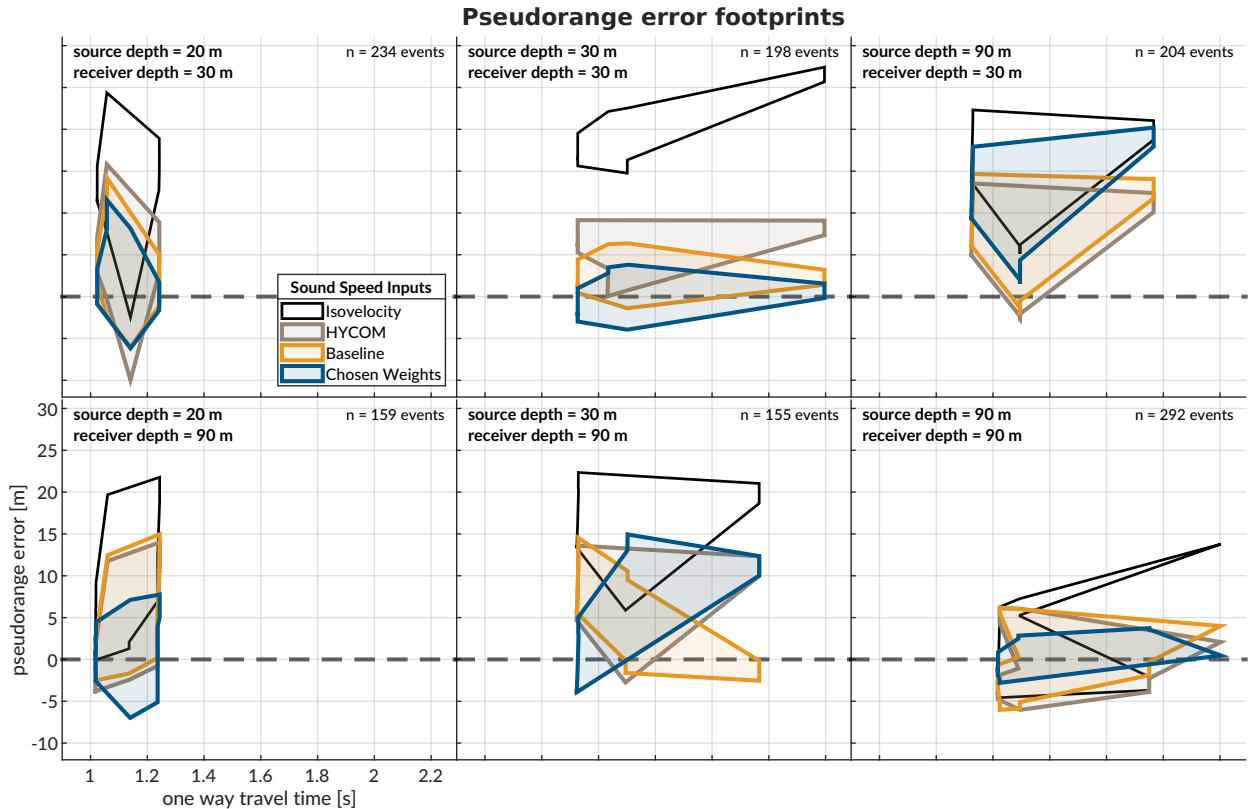


FIG. 10. The post-processed pseudorange error relative to GNSS-derived ranges for all beacon-to-beacon events. The rows share receiver depth; the columns share source depth. The dashed gray line shows no error. The boxed regions connect the pseudorange error across all events.

⁴²⁹ fan is dense enough to resolve eigenrays. All other source depth pairings are significantly
⁴³⁰ improved using the chosen weights compared to HYCOM or baseline SSP.

⁴³¹ When using a range-independent scaling to convert travel time into range, any offset
⁴³² between the assumed and actual sound speed produces unconstrained error with increasing
⁴³³ receiver distance, whereas an adaptive estimate should exhibit no such trend. This is easily
⁴³⁴ observed in the same-layer links, i.e., 30 to 30 m and 90 to 90 m. In cross-layer links, the
⁴³⁵ isovelocity case tends to exaggerate or flip the footprint created adaptively.

436 The improvement from MB to NB is most evident for the data-driven sound speed; while
437 the HYCOM SSP median absolute range error improves from 6.41 to 4.61 m, the baseline
438 SSP one improves from 10.30 to 2.27 m, and the weighted SSP one improves from 13.28
439 to 2.12 m. In comparison, the isovelocity SSP has a median error of 13.09 m. The order
440 of magnitude improvement in the ducted SSPs demonstrates the effectiveness of the NB
441 algorithm exploiting the observed multipath conditions.

442 There is one example that helpfully illustrates the improvement brought upon by bounce
443 classification. For transmissions between North and South at 30 m, the OWTT spread is
444 2.1958 to 2.1963 s; the GNSS-tracked distance is 3138.54 to 3140.87 m; and the implied
445 effective sound speed is 1429.3 to 1430.1 m/s. For these transmissions, the weighted SSP
446 and the MB approach produce a pseudorange error of -1491 m, as the effective sound speed
447 predicted by the minimum bounce criteria is dominated by bottom bounce arrivals with
448 much greater travel times. The NB approach categorizes this same record as a quadruple
449 surface bounce, reducing the pseudorange error to less than a meter. Comparatively, the NB
450 approach for HYCOM and the baseline SSP produce pseudorange errors of 8.30 and 2.39
451 m, respectively. There is strong evidence to suggest that the sound speed and multipath
452 fidelity co-dependently improve localization accuracy.

⁴⁵³ **V. TRILATERATION FOR ICEX20 FIELD DATA**

⁴⁵⁴ To overcome potentially intermittent acoustic communication, the operational paradigm
⁴⁵⁵ of the ICNN computes corrections relative to the trilaterated position estimates transmitted
⁴⁵⁶ by the vehicle, rather than transmitting the updated positions themselves. The reliability
⁴⁵⁷ of the correction is directly linked to how accurately the travel time measurements are
⁴⁵⁸ converted to pseudoranges. This section aims to resolve that tension by reevaluating the
⁴⁵⁹ trilateration results with respect to the MB and NB algorithms. The MB/NB effective
⁴⁶⁰ speed predictions were tracked independently for each source-receiver pair; although the
⁴⁶¹ sound speed was expected to be locally smooth near a given receiver, no such assumption
⁴⁶² was enforced between distinct acoustic links.

⁴⁶³ **A. Re-positioning beacon-to-beacon events**

⁴⁶⁴ When the beacons ran as virtual vehicles, the ICNN did not have access to that buoy's
⁴⁶⁵ GNSS data stream except for what was sent via digital acoustic message. The static nature
⁴⁶⁶ of the experiment means that the initial estimate transmitted to the ICNN was in fact a
⁴⁶⁷ ground truth position. Therefore, a distribution of corrections from the ICNN, as shown in
⁴⁶⁸ Fig. 11, reflects positioning accuracy. The NB, with the median below 3 m rms and mean
⁴⁶⁹ below 6 m rms, clearly outperforms the MB, with the median around 10 m rms and the
⁴⁷⁰ mean above 15 m rms. The 75th percentiles are approximately 5 m rms and 25 m rms,
⁴⁷¹ for the NB and MB, respectively. The MB shows only about 20% within the GNSS puck

⁴⁷² precision; the separate peaks from 9–12 meters and 21–27 meters reflect the distribution of
⁴⁷³ number of surface reflections.

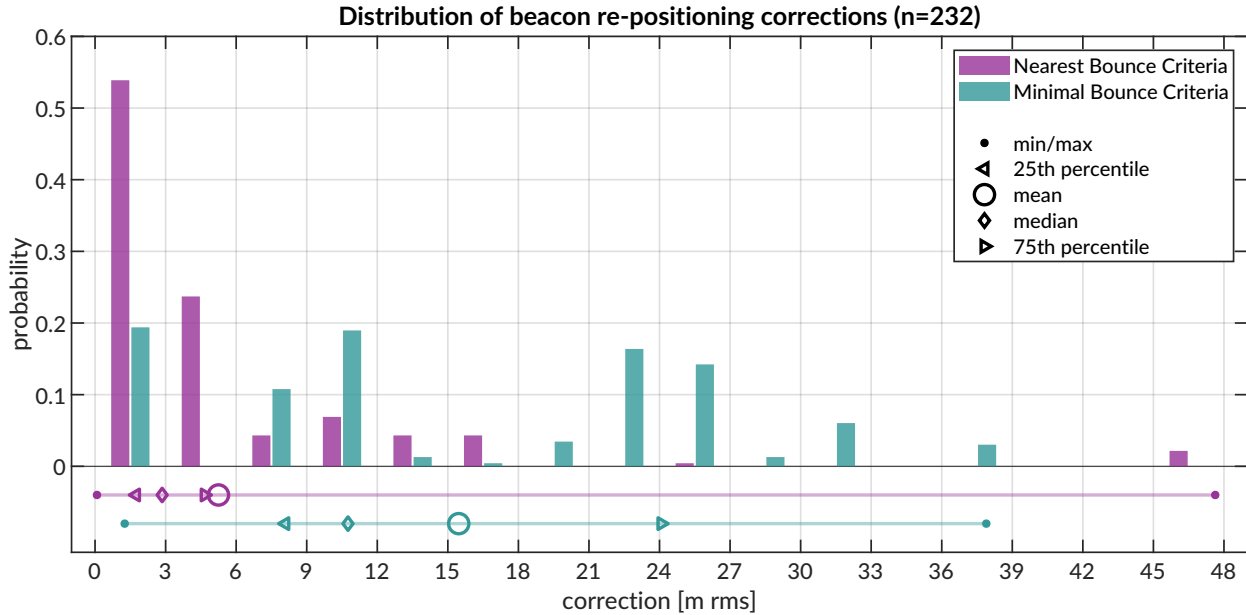


FIG. 11. A histogram (upper) and box plot (lower) of rms correction for trilateration events; 264 entries are two-beacon solutions, 22 are three-beacon, and 2 are four-beacon. For the beacon-to-beacon transmissions, the correction reflects the rms distance between the trilateration solution and the initial position reported by the transmitting buoy. When limited to only two beacons, the trilateration chooses the intersection point closer to the initial position estimate. The precision of the GNSS units used is 3 m. The mean and standard deviation re-positioning corrections for the NB and MB are 5.25 ± 7.60 m rms and 15.47 ± 10.22 m rms, respectively.

⁴⁷⁴ In several events, the MB is unable to accurately estimate the effective sound speed for
⁴⁷⁵ one of the acoustic links, leading to a large positioning error. The NB, however, better
⁴⁷⁶ resolves an approximation of the acoustic path. For example, in some trilateration solutions

⁴⁷⁷ for the Eastern buoy, the MB shows a correction of more than a kilometer; the NB is two
⁴⁷⁸ orders of magnitudes less.

⁴⁷⁹ **B. Re-navigating AUV *Macrura***

⁴⁸⁰ Up to this point, pseudorange estimation and localization have been evaluated on GNSS-
⁴⁸¹ linked beacon-to-beacon connections to validate the NB algorithm. This analysis ports the
⁴⁸² MB and NB algorithms to re-navigate the AUV *Macrura*.

⁴⁸³ In comparison to the modem experiment, the AUV data clearly exhibit instances where
⁴⁸⁴ a receiver detects the same transmission more than once. This is not surprising consider-
⁴⁸⁵ ing the complex multipath provided by the Beaufort Lens. The 11 hour vehicle mission
⁴⁸⁶ contains 3,260 transmissions, 12,938 total detections, and 4,704 successful receptions. Al-
⁴⁸⁷ lowing receptions with PSK errors would almost double the number of recorded multipath
⁴⁸⁸ arrivals exploited for positioning, if a real-time solution could correctly parse paths from
⁴⁸⁹ different arrivals in the same thirty-second cycle. It remains a future endeavor to explore
⁴⁹⁰ how failure mode information from acoustic modems could be used to identify unsuccessful
⁴⁹¹ but otherwise trustworthy arrivals to augment trilateration samples.

⁴⁹² The following performance analysis is constrained to what the vehicle acted on in real-
⁴⁹³ time. AUV *Macrura* and the ICNN ran an adaptive depth behavior to maintain acoustic
⁴⁹⁴ communication on the insight that cross-layer links were more likely to fail than same-layer
⁴⁹⁵ ones. Accordingly, the vehicle dove deeper than 50 meters about 20% of the time it was
⁴⁹⁶ underway. The upper panel of Fig. 12 shows the correction magnitudes for events with three
⁴⁹⁷ or more receptions during AUV operations. Whereas the MB has a fairly bimodal nature,

498 with peaks centered around 10–15 and 35–40 m, the NB favors smaller corrections, from 5–20
 499 m, and has a long tail. In contrast to the modem tests, where position correction illustrated
 500 re-positioning accuracy, the re-navigation corrections are less valuable in the absence of
 501 GNSS ground truth. The correction magnitude necessarily depends on the vehicle’s internal
 502 navigation estimate, which is prone to larger errors from sensor drifts, ocean currents, and
 503 other error not captured in the hydrodynamic model. Thus, larger corrections are not
 504 necessarily indicative of worse performance.

505 Navigation accuracy is better described by trilateration error, the rms of the remaining
 506 pseudorange errors from each acoustic link, shown in the lower panel of Fig. 12. These
 507 errors represent the uncertainty inherent from the overlap of acoustic ranging estimations
 508 and are almost an order of magnitude smaller than the distribution of corrections. The AUV
 509 re-navigation statistics are obtained from three times as many localization events compared
 510 to the beacon-to-beacon dataset. The AUV set also exhibits more events with at least three
 511 beacons and more diverse range-depth pairings. There is strong evidence that both methods
 512 achieve single meter accuracy and that the MB method, with more than 70% of rms error
 513 under 3 m, classifies multipath structure effectively enough to extend GNSS accuracy into
 514 the water column.

515 C. Investigating potential GNSS noise

516

517 The fact that the bulk of the best performing re-navigation error exists within the preci-
 518 sion of the GNSS unit deployed invites a further look into GNSS noise. In the Arctic, GNSS

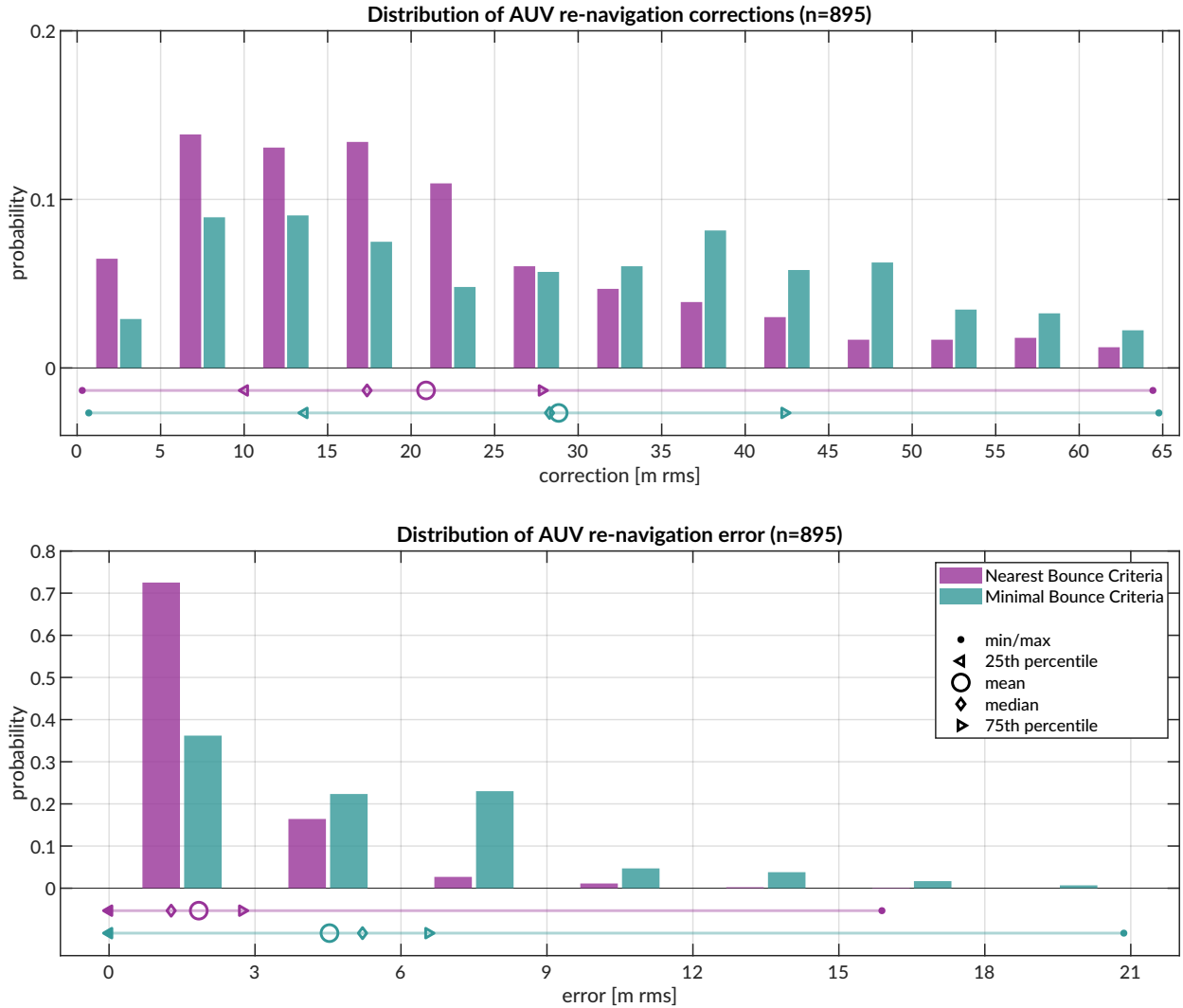


FIG. 12. A distribution of AUV re-navigation rms corrections (top) and rms error (bottom) computed in post-processing for the Minimal and Nearest Bounce Criterion. The re-navigation corrections represent the difference between the initial reported position and the trilateration solution; the mean and standard deviation for the NB and MB are 20.89 ± 14.11 m rms and 28.83 ± 16.79 m rms, respectively. The re-navigation error represents the remaining uncertainty of the trilateration solution; the mean and standard deviation for the NB and MB are 1.84 ± 2.19 and 4.53 ± 4.26 m rms, respectively. The legend of the bottom plot applies to both.

519 performance worsens due to poor constellation coverage, larger ionospheric effects, and mul-
 520 tipath interference (Gwal and Jain, 2011; Jung *et al.*, 2018; National Research Council, 2011;
 521 Reid *et al.*, 2016; Swanlund *et al.*, 2016; Themens *et al.*, 2015). Radio infrastructure that
 522 provides position corrections and references does not regularly extend to polar regions. The
 523 effect is minor for surface platform navigation —roughly 15 m of horizontal precision has
 524 been displayed at the North Pole—but is significant enough to register against the modem’s
 525 detected travel times. Fig. 13 zooms in on the GNSS and OWTT noise relative to the ice
 526 movement for two representative pairs of modem buoy connections. The two panels indicate
 527 the GNSS noise as $\delta R = \sqrt{\delta x^2 + \delta y^2}$ and temporal spread, δt , relative to the median OWTT
 528 recorded between the two modems. The dashed line is scaled by an effective sound speed of
 529 1440 m/s, such that if there were ideal sensor measurements with no drift, all events should
 530 exist on or near the line.

531 The left panel shows the connections between the North and East buoys. The clusters
 532 scaling along the 1440 m/s guideline suggest relative ice movement picked up by both GNSS
 533 and OWTT. But the vertical distribution across many arrival time bands is indicative of
 534 the GNSS fluctuations in precision, or noise. Some minor offsets between these vertical
 535 bands relate to different operational configurations of source and receiver depth. The idea
 536 of GNSS noise relative to OWTT is further indicated by events between two other buoys,
 537 South and West. The relatively thin time window suggests these buoys are moving in
 538 a more rigid ice floe and that there is minimal impact by source and receiver depth on
 539 the spread of OWTT. Yet, the vertical distribution, spanning almost 4 meters, cannot be
 540 explained by time differentials due to acoustic scattering, multipath, and/or environmental

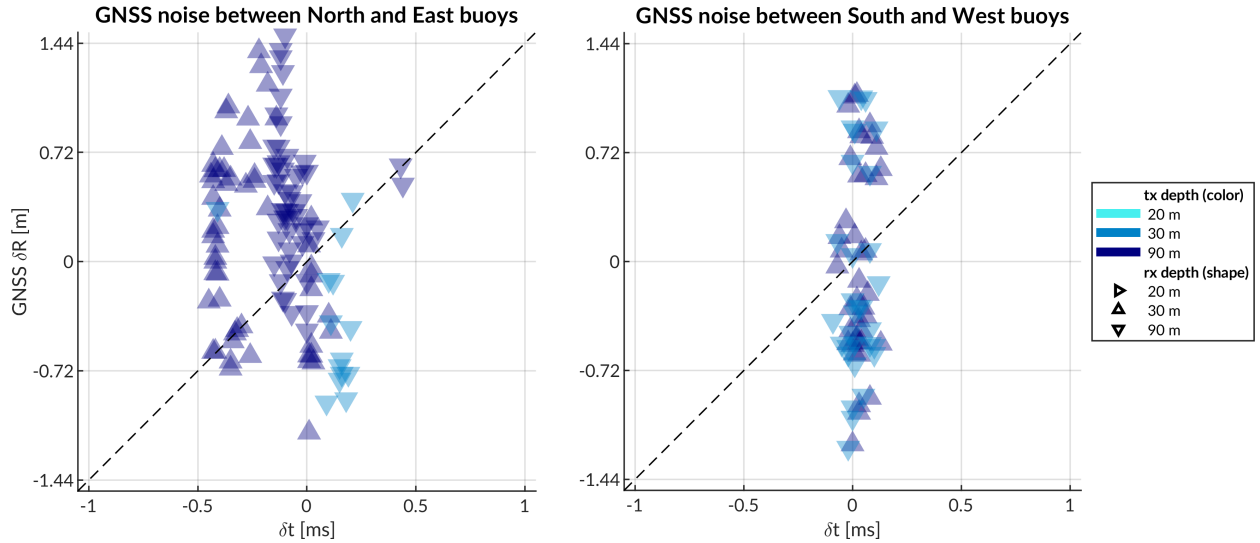


FIG. 13. A comparison of GNSS noise (y-axis) versus OWTT spread (x-axis) between corners of the ICNN network with different source depths. The dashed line normalizes an effective sound speed of 1440 m/s such that the vertical clustering indicates GNSS noise.

541 microstructure. This conclusion corroborates the vertical spread of implied effective speeds

542 in Fig. 9.

543 VI. DISCUSSION

544 Underwater navigation research is broadly motivated by acquiring GNSS-like nava-
545 gation in GNSS-denied conditions. Accurate range estimation is essential to mitigating error.
546 Current approaches for underwater acoustic navigation simplify the non-linear relationship
547 between a SSP and time fronts with a deterministic sound speed. Thus, the conversion of
548 travel time into distance can be pre-conditioned for error and error growth over the course
549 of a vehicle mission.

550 This work introduces a lightweight stochastic prediction of an effective speed along the
551 acoustic path between source and receiver, retooling arrival methods generally deemed too
552 complex or labor intensive for real-time. We assume that the effective sound speed would
553 be a locally smoothly varying function with respect to operational conditions—horizontal
554 and vertical differences and rate of difference between source and receiver. The field-tested
555 approach, the minimal bounce criteria, facilitated a successful AUV recovery in a total
556 ice-covered, double-ducted environment. The accuracy of the MB was validated against
557 GNSS-linked beacon-to-beacon communications. Given a consistent bias towards overesti-
558 mation, an improved algorithm, the nearest bounce criteria, was developed on the insight
559 that multipath structure may play an important role in maintaining a smoothly varying
560 effective sound speed. The NB was developed with field data and reevaluated on vehicle
561 data, achieving a position accuracy and precision that compares with that of the deployed
562 GNSS puck.

563 A key insight for both approaches was seeking an eigenray ensemble around an estimated
 564 location instead of seeking to unambiguously match arrivals. The ensemble diversified the
 565 simulated multipath possibilities to better capture the actual multipath recorded. In this
 566 way, the solution exploits multipath, generally viewed as a source of uncertainty, as a new
 567 dimension of information to improve localization accuracy. Based on the navigation and
 568 re-navigation results of our ice-covered AUV deployment, we conclude that embedding a
 569 model-aided prediction of the effective sound speed has an outsized benefit to minimizing
 570 trilateration error, and that our approach sufficiently resolves the OWTT for an unpre-
 571 dictable and complex propagation environment like the double-ducted Beaufort Lens.

572 There are many avenues through which this approach can be further refined and tested for
 573 field operations. Amongst them is defining the uncertainty grid for BELLHOP via stochastic
 574 or data-driven measures such as the distance traveled by the AUV between ICNN updates
 575 or the magnitude of the position corrections by the ICNN. Another is to entirely remove the
 576 seeded range and instead rely on the submerged asset's depth and recorded OWTT to find
 577 high probability fields in range.

578 The relatively simple nature of this approach invites a discussion about how transferable it
 579 is to other environments, spatio-temporal scales, and platforms. While it is a particular quirk
 580 of the Beaufort Lens that filtering for reflections alone can produce a horizontal effective
 581 speed that compensates for ray refraction and reflection, the algorithm can be reconditioned
 582 to filter against other metrics, like number of turning points, to classify a more diverse and
 583 informed set of multipath features. Though the majority of re-navigation results are within
 584 single-meter accuracy, future work can examine how constellations of more LBL beacons

585 can extend the operational domain without adding an undesirable amount of error. One
 586 possibility is that, during a mission, ICNN-like LBL implementations use a comparison
 587 of the GNSS self-position and acoustic positioning to invert for the ocean volume, linking
 588 how vertical and horizontal sound speed structure impact transmission integrity. A fast
 589 tomographic estimate (Deffenbaugh, 1997; Elisseeff *et al.*, 2002), along with its uncertainty,
 590 could be continuously communicated to assets underway to maintain contact or enable
 591 adaptive sampling. In this sense navigation and tomography converge on the same set of
 592 component technologies—position estimation, sound speed parameterization estimation, ray
 593 path identification, and vehicle path optimization.

594 Spatio-temporal variability is a serious challenge for accurate real-time ranging. For ex-
 595 ample, a recent modeling study showed that eddies and filaments create lateral variability
 596 in the Beaufort Lens (Duda *et al.*, 2021). The effectiveness of the eigenray filtering algo-
 597 rithm is likely challenged by the valid operational scale of a range-independent propagation
 598 environment. One approach to addressing this limitation is to bootstrap filtered eigenrays
 599 for several perturbations of the fitted sound speed profile, which may compensate for oth-
 600 erwise unknowable spatio-temporal variability. Another may be to include range-dependent
 601 ocean snapshots to the eigenray filtering process; this would be necessary for longer range
 602 experiments, which present more spatio-temporal variability but also additional time for
 603 onboard computation. More accurate and higher resolution global circulation models are
 604 needed to properly resolve features that alter ducted propagation at the scales discernible
 605 to an acoustic modem. Through-the-sensor methods can resolve local features but would
 606 require a degree of information sharing not readily supported on the acoustic channel for

607 large scale variability. Addressing the spatial and temporal scales of what can be solved
608 deterministically and what must be solved stochastically imposes a resolution constraint
609 that is at odds with computational overhead for real-time operations. Resolving features
610 inaccurately, or with a false sense of confidence, could be more harmful than contextualizing
611 the limitations of a range independent propagation over realistic bathymetry. Given that
612 AUV operations are often on smaller spatial and temporal scales, the added benefit of an
613 ocean model is quite small, and for features like the Beaufort Lens, not well resolved.

614 The methods involved in this paper include open source software projects ([Benjamin](#)
615 *et al.*, 2010; [Schneider et al., 2015](#); [Schneider and Schmidt, 2010](#)) that are platform agnostic.
616 Large AUVs, often powerful enough to support long duration and/or deep sea missions,
617 would benefit from including diurnal or tidal effects for ranging; eigenray filtering would be
618 simpler given sound speed homogeneity at depth. Gliders, though generally low power and
619 memory, have been equipped with acoustic modems. Their inability to maintain position
620 within a region of reliable acoustic path makes them ripe for environmentally and acoustically
621 adaptive range estimation, where the resource-heavy computation could occur on the LBL
622 network. Ship-based computers can provide the same functionality for short and ultra-short
623 baseline paradigms in large and/or complex acoustic environments. The exact adjustments
624 to the ensemble eigenray filtering are predicated on the expected sound speed conditions
625 and acoustic arrival structure; the problem is well-suited for other simulation testbeds and
626 machine learning classification. The continued development of embedded acoustic processing
627 on and across heterogeneous platforms is fundamental to support a universal underwater
628 navigation scheme comparable to GNSS.

629 **ACKNOWLEDGMENTS**

630 We thank the editors and reviewers for their thoughtful and detailed feedback in im-
 631 proving this work. We also thank all those in the LAMSS ICEX20 team and our collab-
 632 orators from General Dynamics and the WHOI AComms Group. The Ice-Tethered Pro-
 633 filer data were collected and made available by the Ice-Tethered Profiler Program (Toole
 634 et al., 2011; Krishfield et al., 2008) based at the Woods Hole Oceanographic Institution
 635 (www2.whoi.edu/site/itp).

636 Bhatt was a student at the MIT-WHOI Joint Program in Oceanography/Applied Ocean
 637 Science & Engineering, funded by a National Defense, Science, and Engineering Graduate
 638 Fellowship. This work was supported by the Office of Naval Research 322-OA under ICEX20
 639 (N00014-17-1-2474) and Task Force Ocean (N00014-19-1-2716).

640

641 Ballard, M. S., Badiey, M., Sagers, J. D., Colosi, J. A., Turgut, A., Pecknold, S., Lin,
 642 Y.-T., Proshutinsky, A., Krishfield, R., Worcester, P. F., and Dzieciuch, M. A. (2020).
 643 “Temporal and spatial dependence of a yearlong record of sound propagation from the
 644 Canada Basin to the Chukchi Shelf,” The Journal of the Acoustical Society of America
 645 **148**(3), 1663–1680, doi: [10.1121/10.0001970](https://doi.org/10.1121/10.0001970).

646 Barker, L. D., Jakuba, M. V., Bowen, A. D., German, C. R., Maksym, T., Mayer, L.,
 647 Boetius, A., Dutrieux, P., and Whitcomb, L. L. (2020). “Scientific challenges and present
 648 capabilities in underwater robotic vehicle design and navigation for oceanographic explo-

- 649 ration under-ice,” Remote Sensing **12**(16), 1–31, doi: [10.3390/RS12162588](https://doi.org/10.3390/RS12162588).
- 650 Bellingham, J. G., Leonard, J. J., Vaganay, J., Goudey, C. A., Atwood, D. K., Consi,
- 651 T. R., Bales, J. W., Schmidt, H., and Chryssostomidis, C. (**1995**). “AUV operations in
- 652 the Arctic,” in *Proceedings of the Sea Ice Mechanics and Arctic Modeling Workshop*, Vol.
- 653 2, pp. 190–198.
- 654 Benjamin, M. R., Schmidt, H., Newman, P. M., and Leonard, J. J. (**2010**). “Nested au-
- 655 tonomy for unmanned marine vehicles with MOOS-IvP,” Journal of Field Robotics **27**(6),
- 656 834–875, doi: [10.1002/rob.20370](https://doi.org/10.1002/rob.20370).
- 657 Bhatt, E. C. (**2021**). “A Virtual Ocean framework for environmentally adaptive, embed-
- 658 ded acoustic navigation on autonomous underwater vehicles,” Ph.D. thesis, Massachusetts
- 659 Institute of Technology and Woods Hole Oceanographic Institution Joint Program in
- 660 Oceanography/Applied Ocean Science & Engineering, doi: [10.1575/1912/27309](https://doi.org/10.1575/1912/27309).
- 661 Bhatt, E. C., Howard, B., and Schmidt, H. (**2022**). “An Embedded Tactical Decision Aid
- 662 Framework for Environmentally Adaptive Autonomous Underwater Vehicle and Commu-
- 663 nication,” IEEE Journal of Oceanic Engineering (in press).
- 664 Brooke, J. (**1981**). “ARCS (Autonomous remotely controlled submersible),” in *Proceedings*
- 665 *of the 1981 2nd International Symposium on Unmanned Untethered Submersible Technol-*
- 666 *ogy*, IEEE, Vol. 2, p. 28, doi: [10.1109/UUST.1981.1158450](https://doi.org/10.1109/UUST.1981.1158450).
- 667 Chassignet, E. P., Hurlburt, H. E., Smedstad, O. M., Halliwell, G. R., Hogan, P. J.,
- 668 Wallcraft, A. J., Baraille, R., and Bleck, R. (**2007**). “The HYCOM HYbrid Coordinate
- 669 Ocean Model data assimilative system,” Journal of Marine Systems **65**(1), 60–83, doi:
- 670 [10.1016/j.jmarsys.2005.09.016](https://doi.org/10.1016/j.jmarsys.2005.09.016).

- 671 Chen, R., Poulsen, A., and Schmidt, H. (2019). “Spectral, spatial, and temporal character-
672 istics of underwater ambient noise in the Beaufort Sea in 1994 and 2016,” *The Journal of*
673 *the Acoustical Society of America* **145**(2), 605–614, doi: [10.1121/1.5088601](https://doi.org/10.1121/1.5088601).
- 674 Chen, R., and Schmidt, H. (2020). “Temporal and spatial characteristics of the Beaufort
675 Sea ambient noise environment,” *The Journal of the Acoustical Society of America* **148**(6),
676 3928–3941, doi: [10.1121/10.0002955](https://doi.org/10.1121/10.0002955).
- 677 Claus, B., Kepper, J. H., Suman, S., and Kinsey, J. C. (2018). “Closed-loop one-way-travel-
678 time navigation using low-grade odometry for autonomous underwater vehicles,” *Journal*
679 *of Field Robotics* **35**(4), 421–434, doi: [10.1002/rob.21746](https://doi.org/10.1002/rob.21746).
- 680 Deffenbaugh, M. (1997). “Optimal Ocean Acoustic Tomography and Navigation with Mov-
681 ing Sources,” Ph.D. thesis, Massachusetts Institute of Technology.
- 682 Deffenbaugh, M., Bellingham, J. G., and Schmidt, H. (1996a). “The relationship between
683 spherical and hyperbolic positioning,” in *OCEANS 96 MTS/IEEE Conference Proceedings.*
684 *The Coastal Ocean - Prospects for the 21st Century*, Vol. 2, pp. 590–595, doi: [10.1109/OCEANS.1996.568293](https://doi.org/10.1109/OCEANS.1996.568293).
- 686 Deffenbaugh, M., Schmidt, H., and Bellingham, J. G. (1996b). “Acoustic positioning in a
687 fading multipath environment,” in *OCEANS 96 MTS/IEEE Conference Proceedings*, Vol.
688 2, pp. 596–600, doi: [10.1109/OCEANS.1996.568294](https://doi.org/10.1109/OCEANS.1996.568294).
- 689 Duda, T. F., Morozov, A. K., Howe, B. M., Brown, M. G., Speer, K., Lazarevich, P.,
690 Worcester, P. F., and Cornuelle, B. D. (2006). “Evaluation of a Long-Range Joint Acoustic
691 Navigation Thermometry System,” in *OCEANS 2006*, pp. 1–6, doi: [10.1109/OCEANS.2006.306999](https://doi.org/10.1109/OCEANS.2006.306999).

- 693 Duda, T. F., Zhang, W. G., and Lin, Y.-T. (2021). “Effects of Pacific Summer Water layer
 694 variations and ice cover on Beaufort Sea underwater sound ducting,” *The Journal of the*
 695 *Acoustical Society of America* **149**(4), 2117–2136, doi: [10.1121/10.0003929](https://doi.org/10.1121/10.0003929).
- 696 Duda, T. F., Zhang, W. G., Lin, Y.-T., and Newhall, A. E. (2019). “Long-range sound
 697 propagation in the Canada Basin,” in *Proceedings of the Underwater Acoustics Conference*
 698 & Exhibition 2019, pp. 483–490.
- 699 Elisseeff, P., Schmidt, H., and Xu, W. (2002). “Ocean acoustic tomography as a data
 700 assimilation problem,” *IEEE Journal of Oceanic Engineering* **27**(2), 275–282, doi: [10.1109/JOE.2002.1002482](https://doi.org/10.1109/JOE.2002.1002482).
- 701
- 702 Eustice, R. M., Whitcomb, L. L., Singh, H., and Grund, M. (2006). “Recent advances in
 703 synchronous-clock one-way-travel-time acoustic navigation,” in *Oceans 2006*, IEEE, pp.
 704 1–6, doi: [10.1109/OCEANS.2006.306931](https://doi.org/10.1109/OCEANS.2006.306931).
- 705 Eustice, R. M., Whitcomb, L. L., Singh, H., and Grund, M. (2007). “Experimental Re-
 706 sults in Synchronous-Clock One-Way-Travel-Time Acoustic Navigation for Autonomous
 707 Underwater Vehicles,” in *Proceedings 2007 IEEE International Conference on Robotics*
 708 *and Automation*, pp. 4257–4264, doi: [10.1109/ROBOT.2007.364134](https://doi.org/10.1109/ROBOT.2007.364134).
- 709 Fossum, T. O., Norgren, P., Fer, I., Nilsen, F., Koenig, Z. C., and Ludvigsen, M. (2021).
 710 “Adaptive Sampling of Surface Fronts in the Arctic Using an Autonomous Underwater
 711 Vehicle,” *IEEE Journal of Oceanic Engineering* **46**(4), 1155–1164, doi: [10.1109/JOE.2021.3070912](https://doi.org/10.1109/JOE.2021.3070912).
- 712
- 713 Freitag, L., Ball, K., Partan, J., Koski, P., and Singh, S. (2016). “Long range acoustic com-
 714 munications and navigation in the Arctic,” in *OCEANS 2015 - MTS/IEEE Washington*,

- 715 IEEE, pp. 1–5, doi: [10.23919/oceans.2015.7401956](https://doi.org/10.23919/oceans.2015.7401956).
- 716 Gallimore, E., Partan, J., Vaughn, I., Singh, S., Shusta, J., and Freitag, L. (2010). “The
 717 WHOI micromodem-2: A scalable system for acoustic communications and networking,”
 718 in *Oceans 2010 MTS/IEEE Seattle*, IEEE, pp. 1–7, doi: [10.1109/OCEANS.2010.5664354](https://doi.org/10.1109/OCEANS.2010.5664354).
- 719 Graupe, C. E., Van Uffelen, L. J., Webster, S. E., Worcester, P. F., and Dzieciuch, M. A.
 720 (2019). “Preliminary results for glider localization in the Beaufort Duct using broadband
 721 acoustic sources at long range,” in *OCEANS 2019 MTS/IEEE Seattle, OCEANS 2019*,
 722 IEEE, pp. 1–6, doi: [10.23919/OCEANS40490.2019.8962637](https://doi.org/10.23919/OCEANS40490.2019.8962637).
- 723 Gwal, A., and Jain, A. (2011). “GPS scintillation studies in the arctic region during the
 724 first winter-phase 2008 Indian Arctic Expedition,” *Polar Science* **4**(4), 574–587, doi: [10.1016/j.polar.2010.08.001](https://doi.org/10.1016/j.polar.2010.08.001).
- 725 Hayes, D. R., and Morison, J. H. (2002). “Determining turbulent vertical velocity, and
 726 fluxes of heat and salt with an autonomous underwater vehicle,” *Journal of Atmospheric
 727 and Oceanic Technology* **19**(5), 759–779, doi: [10.1175/1520-0426\(2002\)019%3C0759:DTVVAF%3E2.0.CO;2](https://doi.org/10.1175/1520-0426(2002)019%3C0759:DTVVAF%3E2.0.CO;2).
- 729 Howe, B. M., Miksis-Olds, J., Rehm, E., Sagen, H., Worcester, P. F., and Haralabus, G.
 730 (2019). “Observing the Oceans Acoustically,” *Frontiers in Marine Science* **6**(JUL), 1–22,
 731 doi: [10.3389/fmars.2019.00426](https://doi.org/10.3389/fmars.2019.00426).
- 732 Jackson, E. (1983). “Autonomous remotely controlled submersible ”ARCS”,” in *Proceedings
 733 of the 1983 3rd International Symposium on Unmanned Untethered Submersible Technol-
 734 ogy*, IEEE, Vol. 3, pp. 77–88.
- 735

- 736 Jakuba, M. V., Roman, C. N., Singh, H., Murphy, C., Kunz, C., Willis, C., Sato, T.,
 737 and Sohn, R. A. (2008). “Long-baseline acoustic navigation for under-ice autonomous
 738 underwater vehicle operations,” *Journal of Field Robotics* **25**(11-12), 861–879, doi: <https://doi.org/10.1002/rob.20250>.
- 740 Jung, T. S., Hegel, T. M., Bentzen, T. W., Egli, K., Jessup, L., Kienzler, M., Kuba, K.,
 741 Kukka, P. M., Russell, K., Suitor, M. P., and Tatsumi, K. (2018). “Accuracy and per-
 742 formance of low-feature GPS collars deployed on bison *Bison bison* and caribou *Rangifer*
 743 *tarandus*,” *Wildlife Biology* **2018**(1), doi: [10.2981/wlb.00404](https://doi.org/10.2981/wlb.00404).
- 744 Kepper, J. H., Claus, B. C., and Kinsey, J. C. (2017). “MEMS IMU and one-way-travel-
 745 time navigation for autonomous underwater vehicles,” in *OCEANS 2017 - Aberdeen*, IEEE,
 746 Aberdeen, UK, pp. 1–9, doi: [10.1109/OCEANSE.2017.8084842](https://doi.org/10.1109/OCEANSE.2017.8084842).
- 747 Krishfield, R., Toole, J., Proshutinsky, A., and Timmermans, M. L. (2008). “Automated
 748 ice-tethered profilers for seawater observations under pack ice in all seasons,” *Journal of*
 749 *Atmospheric and Oceanic Technology* **25**(11), 2091–2105, doi: [10.1175/2008JTECH0587](https://doi.org/10.1175/2008JTECH0587).
- 750 1.
- 751 Kukulya, A., Plueddemann, A., Austin, T., Stokey, R., Purcell, M., Allen, B., Littlefield, R.,
 752 Freitag, L., Koski, P., Gallimore, E., Kemp, J., Newhall, K., and Pietro, J. (2010). “Under-
 753 ice operations with a REMUS-100 AUV in the Arctic,” in *2010 IEEE/OES Autonomous*
 754 *Underwater Vehicles, AUV 2010*, IEEE, pp. 1–8, doi: [10.1109/AUV.2010.5779661](https://doi.org/10.1109/AUV.2010.5779661).
- 755 Kunz, C., Murphy, C., Camilli, R., Singh, H., Bailey, J., Eustice, R., Jakuba, M., Nakamura,
 756 K. I., Roman, C., Sato, T., Sohn, R. A., and Willis, C. (2008). “Deep sea underwater
 757 robotic exploration in the ice-covered arctic ocean with AUVs,” in *2008 IEEE/RSJ Inter-*

- 758 *national Conference on Intelligent Robots and Systems, IROS*, IEEE, pp. 3654–3660, doi:
759 [10.1109/IROS.2008.4651097](https://doi.org/10.1109/IROS.2008.4651097).
- 760 Light, R. D., and Morison, J. (1989). “The Autonomous Conductivity-Temperture Vehicle:
761 First in the Seashuttle Family of Autonomous Underwater Vehicle’s for Scientific Pay-
762 loads,” in *Proceedings OCEANS*, Vol. 3, pp. 793–798, doi: [10.1109/OCEANS.1989.586683](https://doi.org/10.1109/OCEANS.1989.586683).
- 763 Litvak, A. G. (2015). “Acoustics of the deepwater part of the Arctic Ocean and of Russia’s
764 Arctic shelf,” *Herald of the Russian Academy of Sciences* **85**(3), 239–250, doi: [10.1134/S1019331615030144](https://doi.org/10.1134/S1019331615030144).
- 766 Mikhalevsky, P. N., Sperry, B. J., Woolfe, K. F., Dzieciuch, M. A., and Worcester, P. F.
767 (2020). “Deep ocean long range underwater navigation,” *The Journal of the Acoustical
768 Society of America* **147**(4), 2365–2382, doi: [10.1121/10.0001081](https://doi.org/10.1121/10.0001081).
- 769 National Centers for Environmental Information (2013). “World Ocean Atlas 2009” [https://
770 //www.nodc.noaa.gov/OC5/WOA09/pr_woa09.html](https://www.nodc.noaa.gov/OC5/WOA09/pr_woa09.html).
- 771 National Research Council (2011). *National Security Implications of Climate Change for
772 U.S. Naval Forces* (National Academies Press, Washington, D.C.), doi.org/10.17226/
773 12914.
- 774 Norgren, P., Lubbad, R., and Skjetne, R. (2014). “Unmanned underwater vehicles in Arctic
775 operations,” in *Proceedings of the 22nd IAHR International Symposium on Ice. Singapore*,
776 pp. 89–101.
- 777 Paull, L., Saeedi, S., Seto, M., and Li, H. (2014). “AUV Navigation and Localization: A
778 Review,” *IEEE Journal of Oceanic Engineering* **39**(1), 131–149, doi: [10.1109/JOE.2013.2278891](https://doi.org/10.1109/JOE.2013.2278891).

- 780 Plueddemann, A. J., Kukulya, A. L., Stokey, R., and Freitag, L. (2012). “Autonomous
781 Underwater Vehicle Operations Beneath Coastal Sea Ice,” IEEE/ASME Transactions on
782 Mechatronics **17**(1), 54–64, doi: [10.1109/TMECH.2011.2174798](https://doi.org/10.1109/TMECH.2011.2174798).
- 783 Porter, M. B. (2011). “The bellhop manual and user’s guide: Preliminary draft,” Heat,
784 Light, and Sound Research, Inc., La Jolla, CA, USA, Tech. Rep **260**.
- 785 Poulsen, A. J., and Schmidt, H. (2017). “Acoustic noise properties in the rapidly changing
786 Arctic Ocean,” Proceedings of Meetings on Acoustics (28), 1–10, doi: [10.1121/2.0000552](https://doi.org/10.1121/2.0000552).
- 787 Randeni, S., Schneider, T., and Schmidt, H. (2020). “Construction of a high-resolution
788 under-ice AUV navigation framework using a multidisciplinary virtual environment,” in
789 *2020 IEEE/OES Autonomous Underwater Vehicles Symposium, AUV 2020*, IEEE, pp.
790 1–7, doi: [10.1109/AUV50043.2020.9267950](https://doi.org/10.1109/AUV50043.2020.9267950).
- 791 Reid, T., Walter, T., Blanch, J., and Enge, P. (2016). “GNSS Integrity in The Arctic,”
792 Navigation **63**(4), 469–492, doi: [10.1002/navi.169](https://doi.org/10.1002/navi.169).
- 793 Rossby, T., Dorson, D., and Fontaine, J. (1986). “The RAFOS System,” Journal of
794 Atmospheric and Oceanic Technology **3**(4), 672–679, doi: [10.1175/1520-0426\(1986\)
795 003<0672:TRS>2.0.CO;2](https://doi.org/10.1175/1520-0426(1986)003<0672:TRS>2.0.CO;2).
- 796 Rypkema, N. R., Fischell, E. M., and Schmidt, H. (2017). “One-Way Travel-Time Inverted
797 Ultra-Short Baseline Localization for Low-Cost Autonomous Underwater Vehicles,” in *2017*
798 *IEEE International Conference on Robotics and Automation*, Singapore, pp. 4920–4926,
799 doi: [10.1109/ICRA.2017.7989570](https://doi.org/10.1109/ICRA.2017.7989570).
- 800 Schmidt, H., and Schneider, T. (2016). “Acoustic communication and navigation in the
801 new Arctic — A model case for environmental adaptation,” 2016 IEEE Third Underwa-

- 802 ter Communications and Networking Conference (UComms) 1–4, doi: [10.1109/UComms](https://doi.org/10.1109/UComms).
- 803 [2016.7583469](#).
- 804 Schneider, T., Petillo, S., Schmidt, H., and Murphy, C. (2015). “The dynamic compact
805 control language version 3,” in *OCEANS 2015-Genova*, IEEE, pp. 1–7, doi: [10.1109/OCEANS-Genova.2015.7271608](https://doi.org/10.1109/OCEANS-Genova.2015.7271608).
- 806 Schneider, T., and Schmidt, H. (2010). “Unified command and control for heterogeneous
807 marine sensing networks,” *Journal of Field Robotics* **27**(6), 876–889, doi: <https://doi.org/10.1002/rob.20346>.
- 808 Schneider, T., and Schmidt, H. (2018). “NETSIM: A Realtime Virtual Ocean Hardware-in-
809 the-loop Acoustic Modem Network Simulator,” in *2018 Fourth Underwater Communica-
810 tions and Networking Conference (UComms)*, IEEE, pp. 1–5, doi: [10.1109/UComms.2018.8493188](https://doi.org/10.1109/UComms.2018.8493188).
- 811 Schneider, T., Schmidt, H., and Randeni, S. (2021). “Self-Adapting Under-Ice Integrated
812 Communications and Navigation Network,” in *2021 Fifth Underwater Communica-
813 tions and Networking Conference (UComms)*, IEEE, pp. 1–5, doi: [10.1109/UComms50339.2021.9598012](https://doi.org/10.1109/UComms50339.2021.9598012).
- 814 Singh, S., Grand, M., Bingham, B., Eustice, R., Singh, H., and Freitag, L. (2006). “Un-
815 derwater acoustic navigation with the WHOI Micro-Modem,” in *Oceans 2006*, IEEE, pp.
816 1–4, doi: [10.1109/OCEANS.2006.306853](https://doi.org/10.1109/OCEANS.2006.306853).
- 817 Swanson, D., Maraj, R., Schuurman, N., Hope, R., Donkers, K., Aquin, M., and Rickerby,
818 G. (2016). “GPS performance in Yukon’s Arctic coast,” *Geografiska Annaler: Series A,
819 Physical Geography* **98**(4), 361–368, doi: [10.1111/geoa.12143](https://doi.org/10.1111/geoa.12143).

- 824 Themens, D. R., Jayachandran, P. T., and Langley, R. B. (2015). “The nature of GPS
 825 differential receiver bias variability: An examination in the polar cap region,” Journal of
 826 Geophysical Research: Space Physics **120**(9), 8155–8175, doi: [10.1002/2015JA021639](https://doi.org/10.1002/2015JA021639).
- 827 Timmermans, M.-L., and Winsor, P. (2013). “Scales of horizontal density structure in the
 828 Chukchi Sea surface layer,” Continental Shelf Research **52**, 39–45, doi: [10.1016/j.csr.2012.10.015](https://doi.org/10.1016/j.csr.2012.10.015).
- 830 Toole, J., Krishfield, R., Timmermans, M.-L., and Proshutinsky, A. (2011). “The Ice-
 831 Tethered Profiler: Argo of the Arctic,” Oceanography **24**(3), 126–135, doi: [10.5670/oceanog.2011.64](https://doi.org/10.5670/oceanog.2011.64).
- 833 Van Uffelen, L. J., Howe, B. M., Nosal, E. M., Carter, G. S., Worcester, P. F., and Dzieci-
 834 uch, M. A. (2016). “Localization and subsurface position error estimation of gliders using
 835 broadband acoustic signals at long range,” IEEE Journal of Oceanic Engineering **41**(3),
 836 501–508, doi: [10.1109/JOE.2015.2479016](https://doi.org/10.1109/JOE.2015.2479016).
- 837 Van Uffelen, L. J., Nosal, E.-M., Howe, B. M., Carter, G. S., Worcester, P. F., Dzieciuch,
 838 M. A., Heaney, K. D., Campbell, R. L., and Cross, P. S. (2013). “Estimating uncertainty
 839 in subsurface glider position using transmissions from fixed acoustic tomography sources,”
 840 The Journal of the Acoustical Society of America **134**(4), 3260–3271, doi: [10.1121/1.4818841](https://doi.org/10.1121/1.4818841).
- 842 Van Uffelen, L. J. V. (2021). “Global Positioning Systems: Over Land and Under Sea,”
 843 Acoustics Today **17**(1), 52–60, doi: [10.1121/AT.2021.17.1.52](https://doi.org/10.1121/AT.2021.17.1.52).
- 844 Webster, S. E., Eustice, R. M., Singh, H., and Whitcomb, L. L. (2009). “Preliminary
 845 deep water results in single-beacon one-way-travel-time acoustic navigation for underwater

- 846 vehicles,” in *2009 IEEE/RSJ International Conference on Intelligent Robots and Systems*,
847 *IROS 2009*, IEEE, pp. 2053–2060, doi: [10.1109/IROS.2009.5354457](https://doi.org/10.1109/IROS.2009.5354457).
- 848 Webster, S. E., Eustice, R. M., Singh, H., and Whitcomb, L. L. (2012). “Advances in single-
849 beacon one-way-travel-time acoustic navigation for underwater vehicles,” *The International*
850 *Journal of Robotics Research* **31**(8), 935–950, doi: [10.1177/0278364912446166](https://doi.org/10.1177/0278364912446166).
- 851 Webster, S. E., Freitag, L. E., Lee, C. M., and Gobat, J. I. (2015). “Towards real-time
852 under-ice acoustic navigation at mesoscale ranges,” in *Proceedings - IEEE International*
853 *Conference on Robotics and Automation*, IEEE, Vol. 2015-June, pp. 537–544, doi: [10.1109/ICRA.2015.7139231](https://doi.org/10.1109/ICRA.2015.7139231).
- 855 Wu, M., Barmin, M. P., Andrew, R. K., Weichman, P. B., White, A. W., Lavely, E. M.,
856 Dzieciuch, M. A., Mercer, J. A., Worcester, P. F., and Ritzwoller, M. H. (2019). “Deep
857 water acoustic range estimation based on an ocean general circulation model: Application
858 to PhilSea10 data,” *The Journal of the Acoustical Society of America* **146**(6), 4754–4773,
859 doi: [10.1121/1.5138606](https://doi.org/10.1121/1.5138606).